



Original Paper

Pore Structure Characteristics and Evaluation of Carbonate Reservoir: A Case Study of the Lower Carboniferous in the Marsel Exploration Area, Chu-Sarysu Basin

Kanyuan Shi,^{1,2} Xiongqi Pang,^{1,2,7} Junqing Chen,^{1,3,4,7} Shasha Hui,^{1,2} Wu Yuan,⁵ Jianping Chen,⁵ Tao Hu,^{1,2} Min Li,^{1,2} Kun Zhang,⁶ Yang Liu,^{1,2} Siyu Zhang,^{1,2} and Tingting You^{1,2}

Received 28 July 2022; accepted 19 January 2023
Published online: 15 February 2023

The pore structure of a carbonate reservoir determines the fluidity and storage characteristics of hydrocarbon, and it is vital for reservoir evaluation and oil and gas production. The Visean and Serpukhovian carbonate reservoirs in the Marsel exploration area of the Chu-Sarysu Basin possess a complex lithology and pore structure, which significantly affect production efficiency. The pore structure of the reservoirs was investigated in this study via X-ray diffraction, conventional petrophysical measurements, cast thin section analysis, scanning electron microscopy (SEM), imaging logging, and high-pressure mercury injection (HPMI). The findings show that the lithology in this area mainly comprises fine-grained limestone, bioclastic limestone, and silty limestone; moreover, the mineral assemblage in this region is markedly different. The types of carbonate reservoir pore spaces are complex and diverse. Primary pores are mainly biological cavity pores with small pore size, mostly isolated individuals, poor connectivity, and weak percolation capacity. Secondary dissolution pores, which are dominated by intergranular dissolution pores, intragranular dissolution pores, and microfractures, are the dominant storage spaces in the Carboniferous carbonate reservoirs. Through an innovative approach of combining imaging logging and cast thin section analysis, it was concluded that mainly three types of fractures exist, namely conductivity fractures, fissures, and resistive fractures. Moreover, structural fractures in this area are relatively developed, which substantially increases the percolation capacity of the reservoirs and it is conducive to oil and gas flow. However, some structural fractures are filled with calcite, destroying the effectiveness of the fractures and reducing the percolation capacity. Based on capillary pressure curves, the samples were divided into three types, of which the physical properties decrease in the order of type I > type III > type II. The fractal dimensions obtained from HPMI and SEM data characterize the complexity of the reservoir microstructure in the study area. The formation of high-porosity and high-permeability zones was caused by quasi-syngenetic dolomitization and syngenetic–quasi-syngenetic dissolution. In this study, the pore structure of carbonate reservoirs in the area was evaluated quantitatively, which is highly significant to improving oil and gas recovery.

KEY WORDS: Chu-Sarysu Basin, Carbonate reservoir, Pore structure, Fractal dimension.

¹State Key Laboratory of Petroleum Resources and Prospecting, China University of Petroleum, Beijing 102249, China.

²College of Geosciences, China University of Petroleum, Beijing 102249, China.

³Beijing Key Laboratory of Optical Detection Technology for Oil and Gas, China University of Petroleum, Beijing 102249, China.

⁴Basic Research Center for Energy Interdisciplinary, College of

Science, China University of Petroleum, Beijing 102249, China.

⁵PetroChina Liaohe Oilfield Company, Panjin 110316, China.

⁶Department of Earth Sciences, University College London, Gower Street, London WC1E 6BT, UK.

⁷To whom correspondence should be addressed; e-mail: pangxqcup@163.com, chenjq@cup.edu.cn

INTRODUCTION

The wide distribution and substantial exploration potential of carbonate reservoirs have attracted the research interest of many geological scientists (Li et al., 2020a, 2020b; Chen et al., 2022). Carbonate rocks are characterized by wide distribution, multiple rock types, rapid phase transformation, and general dolomitization (Wei et al., 2022). For carbonate rocks, researchers have conducted numerous studies from various aspects including sedimentary rhythm, lithofacies combination, hydrocarbon source rock evaluation, reservoir space, and seepage characteristics. These studies indicate that carbonate rocks are both source rocks and reservoirs as well as important areas of tight oil and shale oil exploration (Hamd et al., 2022; Rashid et al., 2022). However, as carbonate reservoirs are mainly affected by sedimentation and diagenesis, their heterogeneity is very strong, generating a very complex pore structure (Jarvie et al., 2007; Wang et al., 2020a, 2020b; Tan et al., 2021). The complexity of pore structure determines the fluidity of oil and gas. Hence, determining the complexity of pore structure is crucial for reservoir evaluation (Liu et al., 2020; Zhang et al., 2020a, 2020b, 2020c; Hu et al., 2022a, 2022b; Pan et al., 2022; Shi et al., 2022). Moreover, since 2013, after occupying the Marsel exploration area in the Chu-Sarysu Basin, Geo-Jade Petroleum Corporation partnered with the China University of Petroleum (Beijing) to conduct numerous exploratory well deployments and experimental studies to obtain a deeper understanding of the carbonate reservoirs in this area. However, the related results were rarely reported. Therefore, summarizing and evaluating the pore structure characteristics quantitatively in this area is necessary.

Currently, several methods are available for studying the pore structure characteristics of carbonate rocks. For example, x-ray diffraction (XRD) is used to analyze mineral composition (Li et al., 2020a, 2020b; Yang et al., 2020). Casting thin section analysis and SEM can be used to identify lithology, pore throat type, and connectivity (Dou et al., 2018; Wang et al., 2019). High-pressure mercury injection (HPMI) can be used to quantitatively determine nitrogen adsorption, carbon dioxide adsorption, pore volume, and pore throat characteristics as well as to obtain fractal dimension (Mastalerz et al., 2017; Chang et al., 2021; Zhou et al., 2021). Fractal

dimension theory can then be used to determine the complexity of pore network and the contribution of various pore parameters to pore heterogeneity (Sahouli et al., 1996; Fu et al., 2017; Hassan et al., 2020). Computed tomography (CT) scanning can distinguish pore types, simulate fluid flow in pore spaces, and demonstrate the spatial characteristics of pore spaces and fractures using a three-dimensional perspective (Sok et al., 2010; Zhang et al., 2022). Imaging logging can characterize natural fractures and identify their characteristics and occurrence (Aghli et al., 2018; Xu et al., 2020). The aforementioned methods adopt different principles; hence their applications differ. Considerable errors will be encountered if only a single method is used to analyze pore structure characteristics (Hu et al., 2020). Therefore, various methods are used in this study to characterize pore structures comprehensively.

Mandelbrot (1975) proposed the fractal theory (Degiorgio et al., 1984; Brandano and Civitelli, 2007). Several theoretical and experimental studies have shown that the pore structures of a reservoir possess fractal properties. Fractal theory can thus be used to describe pore structures quantitatively, and it is an important parameter in describing rock pore evolution and studying pore properties and throat characteristics (Lai and Wang, 2015; Sakhaee-pour and Li, 2016; Li et al., 2017). Currently, the fractal dimension obtained through HPMI is 2–3. The closer it is to 3, the stronger the heterogeneity is. The closer it is to 2, the weaker the heterogeneity is (Pan et al., 2021). The carbonate rocks in the Marsel exploration area are tight reservoirs; hence, HPMI has been used to analyze the fractal characteristics of the tight rocks. HPMI allows good characterization of the fractal properties of pore throats and connected pores; it has thus become the preferred method for calculating the fractal dimension of pore structures (Li et al., 2010, 2020a, 2020b; He et al., 2016; Zambrano et al., 2017). In addition, as high-resolution pore image data acquisition is more intuitive, convenient and statistically more representative, it is widely used to characterize pore fractal dimension quantitatively (Peng et al., 2011; Xu et al., 2014a, 2014b). Xie et al. (2010) used SEM images to systematically describe the micropore structure of a carbonate reservoir through fractal and multifractal methods. Qin et al. (2021) used fractal and multifractal methods to characterize quantitatively different structures of vesicular andesite reservoir samples, providing a basis for predicting high-quality reservoirs. Xin et al. (2022) used

fractal dimension to characterize the pore structure characteristics of ultradeep and dense reservoirs quantitatively based on nuclear magnetic resonance T_2 spectrum data. Recently, it has gradually developed from a typical two-dimensional pore quantitative characterization to the application of multifractal parameters to a three-dimensional micropore description (Xie et al., 2010; Zhang et al., 2020a, 2020b, 2020c; Qin et al., 2021; Xin et al., 2022). Therefore, HPMI data and SEM images were used in this study to analyze the fractal dimension of regional reservoir pore structure.

The foregoing discussion shows that research on pore structure characteristics of carbonate reservoirs in the Marsel exploration area is lacking. Herein, the mineral composition and pore throat characteristics were first analyzed via conventional core photos, XRD, SEM, and HPMI. Moreover, the pore structure characteristics were characterized qualitatively, semiquantitatively, and quantitatively. Imaging logging and casting thin section analysis were used innovatively to analyze the shape and characteristics of fractures; the fractal dimensions obtained through SEM and HPMI were used to study the heterogeneity of pore structure. The influence of fractal dimension on pore structure parameters is then discussed. Finally, the formation mechanism of the high-porosity and high-permeability zone in the study area is discussed. Therefore, a new understanding of the pore structures of carbonate reservoirs in this area and in other areas is presented in this study, facilitating the hydrocarbon development of carbonate reservoirs.

GEOLOGICAL SETTING

The Chu-Sarysu Basin, which is a typical inland basin, is located in the south-central part of Kazakhstan. There are several structural units in the basin, and the basin area reaches 16×10^4 km² (Brunet et al., 1999; Jaireth and Hustone, 2010; Pang et al., 2016; Fig. 1b). The basin is a long strip that is roughly distributed in the NW–SE direction, wide in the west and narrow in the east.

The Marsel exploration area, measuring 1.85×10^4 km², has a square distribution in the southwestern region of the Chu-Sarysu Basin, spanning the Kokpansor Depression and the Suzak Baykadam Depression (Bykadorov et al., 2003; Zhao et al., 2017a, 2017b; Zhang et al., 2020a, 2020b, 2020c; Fig. 1a). Based on its structural style and

characteristics, the interior of the Marsel exploration area can be divided into three small areas (Fig. 1a), namely, the squeeze uplift zone in the east, which is characterized via deep and large faults close to the basement; the stratum, which is strongly uplifted and denuded; and a series of developed NW-trending reverse faults. Presently, the Marsel exploration area is the key natural gas exploration field in the Chu-Sarysu Basin. Its west and northwest host slope depression zones with gentle strata that exhibit weak uplift and denudation. A small number of NE-trending reverse faults are developed, and strong dolomitization and dissolution are developed in some areas, which are potential carbonate gas reservoir exploration targets. To the south is the uplift slope zone, in which the stratum has been uplifted and denuded. Moreover, a series of NW-trending reverse faults and normal faults have been developed, resulting in the formation of fault-nose and fault-anticline structures. The overall exploration degree of the area is low (Zhang et al., 2018).

The basement of the Chu-Sarysu Basin comprises lower Paleozoic metamorphic crystalline rock, and the sedimentary caprock includes the upper Paleozoic, Mesozoic, and Cenozoic (Bykadorov et al., 2003). Of these, the upper Paleozoic is the main caprock system of the basin and the main oil-bearing reservoir system. Therefore, the main target layer of this study is the Lower Carboniferous (Fig. 1d), which contains the Tournasian (C_{1t}), Visean (C_{1v}), and Serpukhovian (C_{1sr}) stages from bottom to top. The Visean stage is the Mississippi stage, with a time limit of 346.7–330.9 Ma. This set of strata can be divided into three sets of stratigraphic units, C_{1v1} , C_{1v2} , and C_{1v3} , from bottom to top. The C_{1v1} stratum is approximately 55–125 m and contains primarily limestone. The C_{1v2} stratum is approximately 50–190 m, with limestone developed at the top and bottom, marl with high argillaceous content, and argillaceous crystal limestone developed at the bottom. The C_{1v3} stratum is approximately 45–140 m, comprising mainly argillaceous limestone and dark-gray micritic limestone. The Serpukhovian stage is the Late Mississippian deposit with an age range of 330.9–323.2 Ma. The overall thickness of the stratum is approximately 100–200 m (Cook et al., 2007; Pang et al., 2014). Based on the differences in its main lithofacies characteristics, it can be divided into four sections from bottom to top: the lowermost reef section, which is mainly marl; reef limestone, which is the main lithofacies of the reef limestone section; gran-

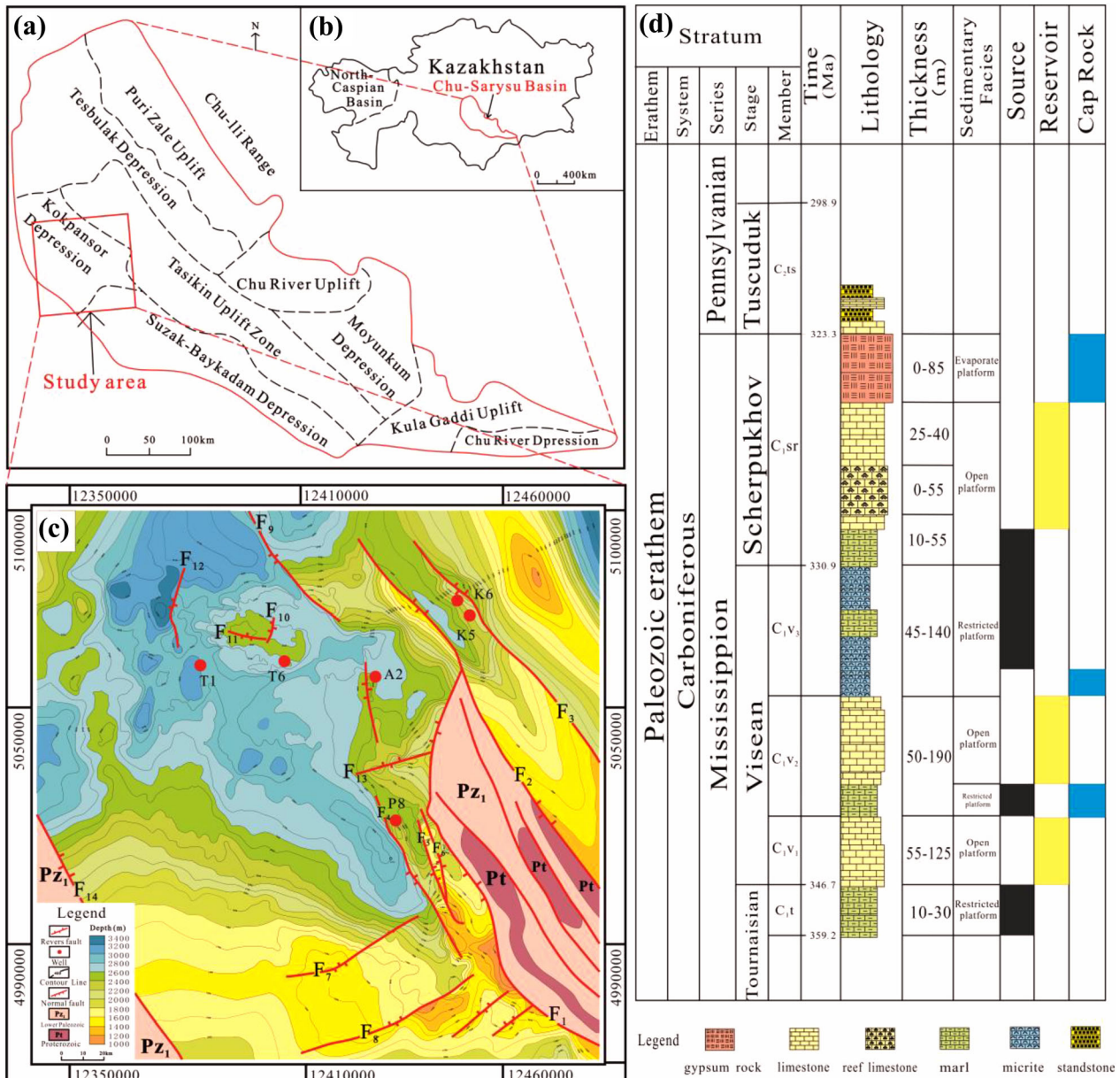


Figure 1. Geographical location maps of the (a) Marsel exploration area and (b) Chu-Sarysu Basin, Kazakhstan. (c) Top structure of the Carboniferous system in the Marsel exploration area. (d) Comprehensive stratigraphic histogram of the Chu-Sarysu Basin, Kazakhstan (modified from Zhao et al., 2017a, 2017b; Li et al., 2018; Zhang et al., 2018).

ular limestone, which is developed in the lower segment of gypsum salt rock; and the evaporite section, which comprises mainly gypsum, anhydrite, salt rock, and other lithofacies. The main source rocks are distributed mainly in C_{1v} and C_{1sr}, with a wide distribution area and large thickness. The lithology contains limestone that is approximately 160–405 m thick (Xu et al., 2014a, 2014b; Li et al., 2018).

SAMPLES AND METHODS

Samples

From six wells (A2, K5, K6, P18, T6, and T1) in the study area, 226 core samples were collected, and plunger samples were made. All samples were collected from carbonate rocks in the C_{1sr} and C_{1v} horizons. Figure 1c shows the location of each well.

Of the collected samples, 226, 10, 13, and 18 samples were tested via conventional petrophysical measurements and cast thin section analysis, XRD, SEM, and HPMI, respectively. All tests were conducted at the Central Asia Institute of China Exploration and Development Research Institute. In addition, imaging logging of well A2 was performed by the Schlumberger Company to study its fracture characteristics.

Experimental Methods

A D8 ADVANCE X-ray diffractometer was used to identify the whole-rock minerals of 10 samples, and the contents of various mineral components and clay minerals in sedimentary rocks were obtained. Samples were crushed to 200 mesh before the experiment. The scanning speed of the instrument, the step size, and angle range were 2°/min, 0.02°, and 2°–60°, respectively (Zhou et al., 2021). The porosity and permeability of 226 samples were measured using an ES-V gas permeability meter. Porosity was determined via the helium expansion method, and the permeability was determined by measuring the air flowing through the sample. An Axioskop 40 POL polarizing microscope was used to determine the cast thin section analysis of 12 samples. Prior to the experiment, the sample was dyed with blue epoxy resin and quantitatively analyzed using a CIAS-2007 image analyzer (Chang et al., 2021). A Zeiss EVO MA15 scanning electron microscope was used to analyze and test the 14 samples. Before the experiment, the samples were cut into dimensions of 1 × 1 × 0.5 cm and polished with an argon ion beam for observation (Qiao et al., 2022). A 9505 mercury porosimeter was used to test the 18 samples. Prior to the test, the samples were cleaned with ethanol, dried, and placed into the head of the measuring instrument, before applying different pressures to force mercury to enter the pores. Mercury inlet saturation was recorded under different pressures to obtain a series of parameters, including mercury inlet saturation, sorting coefficient, and pore volume. The imaging logging data were normalized statically and dynamically to generate high-resolution color images. Different image colors can reflect fluid complexity (Lai et al., 2018a, 2018b; Wang et al., 2020a, 2020b). Subsequently, the Techlog software was used to fit the sinusoidal curve and manually characterize the cracks (Lai et al., 2018a, 2018b).

Theory of Calculating Fractal Dimension by HPMI

Currently, several experimental models and methods, including the thermodynamic, Frenkel–Halesy–Hill, and Brunauer–Emmett–Teller models, are used to calculate fractal dimension (Pfeifer, 1990; Yang et al., 2014; Jiang et al., 2016; Zhao et al., 2017a, 2017b; Wang et al., 2018). Of these, the gas adsorption method of the Frenkel–Halesy–Hill model has proven to be the most effective method (Pfeifer, 1990; Sun et al., 2016).

During the experiments, interfacial tension is generated when immiscible liquids come in contact, and the pressures on both sides are not equal. The liquid with a concave liquid surface bears greater pressure than the contact liquid. This pressure difference is called capillary pressure (P_c), which is expressed as:

$$P_c = P_{nw} - P_w \quad (1)$$

where P_{nw} represents the pressure borne by the nonwetting-phase fluid, and P_c and P_w represent the internal pressure of the wetting-phase fluid, MPa. P_c can be calculated according to Laplace's equation as:

$$P_c = \sigma_L \left(\frac{1}{R_1} + \frac{1}{R_2} \right) \quad (2)$$

where σ_L represents the interfacial tension (N/m), and R_1 and R_2 represent the principal radii (m) of curvatures of a point on the curved surface. For an equal-diameter capillary with $R_1 + R_2 = R$ and $r = R \cos \theta$, Eq. 2 can be expressed as:

$$P_c = \frac{2\sigma_L \cos \theta}{r} \quad (3)$$

where θ is the wetting contact angle (°), and r is the capillary radius (m). Equation 3 gives the main formula for analyzing a mercury injection curve. The formula used to calculate the fractal dimension using mercury injection data is derived as:

$$S_w = \left(\frac{P_c}{P_{\min}} \right)^{D_1 - 3} \quad (4)$$

where P_{\min} is the capillary pressure (MPa) that corresponds to the maximum pore throat radius of the reservoir rock, and S_w is the saturation (%) of the reservoir rock. This formula is converted to logarithmic form to obtain:

$$\lg S_w = (D_1 - 3) \lg P_c - (D_1 - 3) \lg P_{\min} \quad (5)$$

As shown in Eq. 5, $\lg S_w$ and $\lg P_c$ exhibit good correlation when the pore structure of a reservoir rock has fractal characteristics. Moreover, if the two are linearly correlated, the pore fractal dimension D_1 can be obtained using the slope of the line.

First, HPMI experiments were performed on the core to obtain mercury injection data. The obtained data were then processed according to Eq. 5. Finally, the data points in the scatter diagram were linearly fitted. For fractal cores, D_1 was calculated using the slope $K = D_1 - 3$. The closer the fractal dimension is to 3, the lower is the fractal fitting degree (Jiang et al., 2016).

According to Eq. 5, D_1 can be obtained, which is calculated using the slope of a straight line fitted using all logarithmic scatter points. According to the curve shape of the scatter diagram, the fractal dimension D of the piecewise linear regression is piecewise fitted, and D_2 and D_3 are calculated. D is calculated as:

$$D = D_2 \cdot S'_w + D_3 \cdot (S - S'_w) \quad (6)$$

where S'_w is the saturation (%) of wet facies in the coarse pore throat of a reservoir rock D is the fractal dimension of the piecewise linear regression, D_1 is the overall linear regression fractal dimension of the core pore structure, D_2 is the fractal dimension of the coarse pore throat, D_3 is the fractal dimension of the fine pore throat, and S is the maximum mercury saturation (%) of the core.

Theory of Calculating Fractal Dimension by SEM

From the perspective of image analysis, high-resolution pore images are obtained via SEM, and pore structure parameters are counted quantitatively to evaluate the characteristics of pore heterogeneity (Xie et al., 2010; Peng et al., 2011; Xu et al., 2014a, 2014b; Qin et al., 2021). In this study, a professional image processing software, JMicroVision, was used to obtain pore structure parameters quantitatively from SEM images. It is a powerful image acquisition, processing, and analysis software that can extract the perimeter, area, number of pores, and other parameters of different regions and types of pores, making it very convenient and effective.

The high-resolution image obtained via SEM is a grayscale image, which can identify different types of pores. Distinguishing pores from the skeleton is

necessary to obtain the pore structure parameters quantitatively. Threshold segmentation is the most commonly used pore segmentation method, which is performed mainly in two steps. First, a reasonable threshold is determined. Pixels with a gray value less than the threshold in the image are then divided into pores, and those with a gray value greater than the threshold are divided into backgrounds (Xu et al., 2014a, 2014b). Based on the above steps and fractal theory, the pore fractal dimension can be calculated.

Previous research results indicate that if the pore morphology in a sample image has fractal characteristics, the pore area and its equivalent perimeter have the following relationship (Voss et al., 1991):

$$\lg P = \frac{D_0}{2} \lg S + C \quad (7)$$

where P and S are the equivalent perimeter and area of any polygon in the image, C is a constant, and D_0 is the fractal dimension of pore morphology that correspond to the image.

RESULTS

Mineral Composition

Based on the XRD analysis results obtained for the samples, it was concluded that the content of different minerals in the target reservoir considerably changes. Calcite was the main mineral type, constituting 38.0% of all minerals (Fig. 2a), with dolomite, quartz, and feldspar contents of 22.7%, 21.6%, and 12.1%, respectively. The content of pyrite and clay minerals was less in a single rock sample. The content of clay minerals ranged from 0.84 to 7%, among which the content of illite/smectite mixed layers (I/S) was the highest (41.2%), followed by illite (35.5%), and chlorite (23.3%). Kaolinite or montmorillonite was not detected in the sample (Fig. 2b).

Conventional Petrophysical Measurements

A very poor correlation was observed between the porosity and permeability of carbonate samples in the study area, which were both generally low (Fig. 3a). This indicates that the entire pore network controls permeability. Owing to the development of microfractures, the permeabilities of some samples

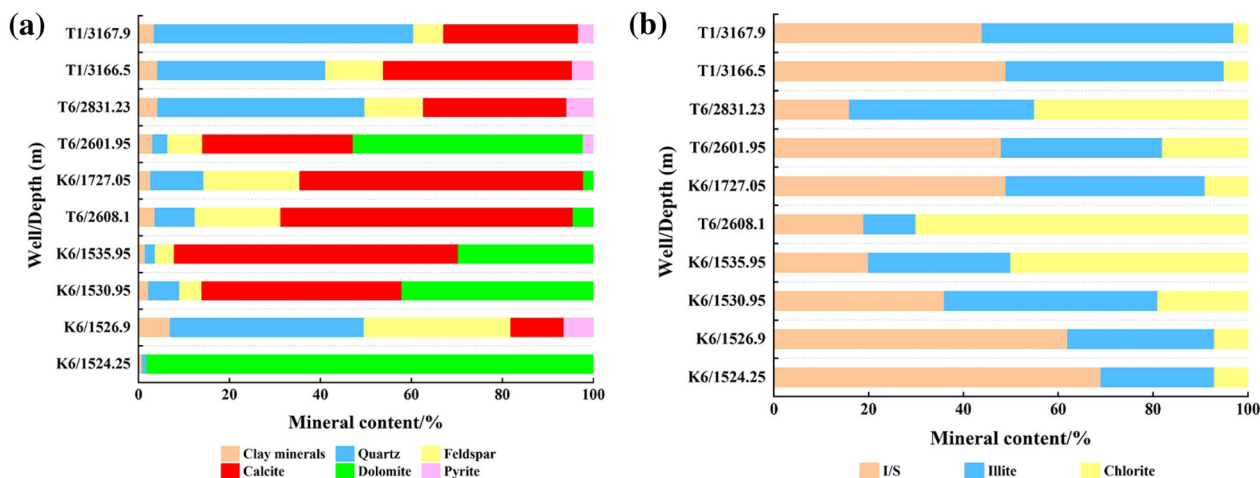


Figure 2. (a) Mineral and (b) clay composition of the 10 samples (some data from Zhang et al., 2018).

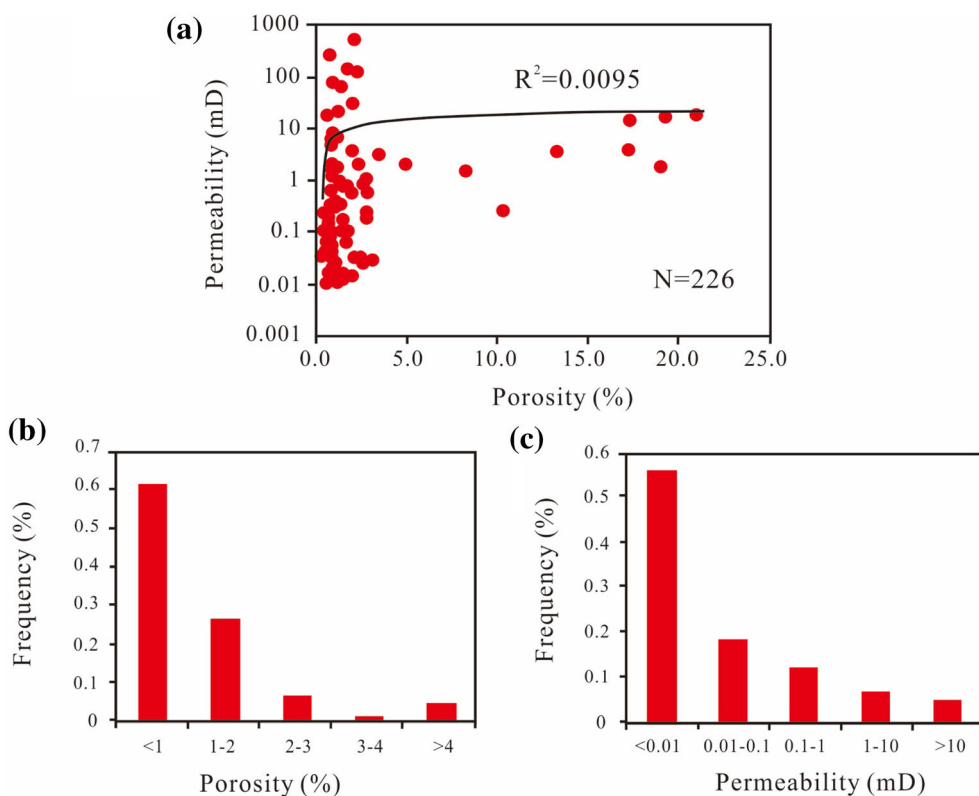


Figure 3. (a) Intersection diagram of porosity and permeability. (b) Porosity distribution histogram. (c) Permeability distribution histogram.

were abnormally high, and those of samples without microfractures were mostly < 0.1 mD.¹ Generally, this is because different sedimentary environments determine the difficulty of carbonate reservoir

reconstruction in the process of later diagenesis and tectonic movement. Moreover, it controls the formation and spatial combination of pores, fractures, and karst caves, which result in a complex pore

¹ * 1 mD = 1 millidarcy = 9.86923 × 10⁻¹⁵ m².

permeability relationship of the carbonate reservoir (Westphal et al., 2004; Haines et al., 2016).

The porosity of the samples ranged from 0.1 to 20.8%, of which 61.5% samples had a porosity of < 1% (Fig. 3b). The average permeability was 14.10 mD (Fig. 3c). Most samples were very dense; however, the maximum porosity and permeability reached 20.8% and 18.8 mD, respectively, in well K6 with a depth of 1522.85–1525.05 m. Overall, carbonate rocks can be classified as tight reservoirs; however, they have some high-porosity and high-permeability zones (their genesis is described in detail below in Section “Causes of High-Porosity and High-Permeability Zones”). Overall, according to the oil and gas industry standard of the People’s Republic of China: Oil and gas reservoir evaluation method (SY/T 6285-2011) drafted by Ren et al. (2011), the reservoir in this area is an ultralow-porosity and ultralow-permeability carbonate reservoir.

Pore Characteristics

Pore Characteristics by Core Observation

The core observations showed that most cores were dense and of a cryptocrystalline structure (Fig. 4) with highly developed fractures (Fig. 4a and h). Calcite (Fig. 4c) and anhydrite (Fig. 4e and h) commonly filled the fractures. The specific characteristics of each core photo are as follows: from Figure 4a, a sawtooth suture structure can be seen, and two discontinuous straight split fractures can be seen in the middle with maximum fracture width of 2 mm and maximum length of 10 cm, which were fully filled with white gypsum. The crystal cave filled with other crystal gypsum can be seen sporadically, the maximum crystal cave being 2×50 mm, and a small amount of bioclastic fossils is irregularly distributed in the whole section (Fig. 4b). As shown in Figure 4c, a large karst cave can be seen in the middle with dimensions of 80×100 mm, which is fully filled with white euhedral crystal calcite. Figure 4d shows a wavy suture structure. As shown in Figure 4e, there is a middle hole at 0.35 m from the top with size of 4×10 cm, which is fully filled with gypsum. As shown in Figure 4f, 1.01 m away from the top, there is a middle hole with size of 4×6 cm, which is fully filled with mud. As shown in Figure 4g, the argillaceous limestone exhibits horizontal bedding. As shown in Figure 4h, there are two distinct

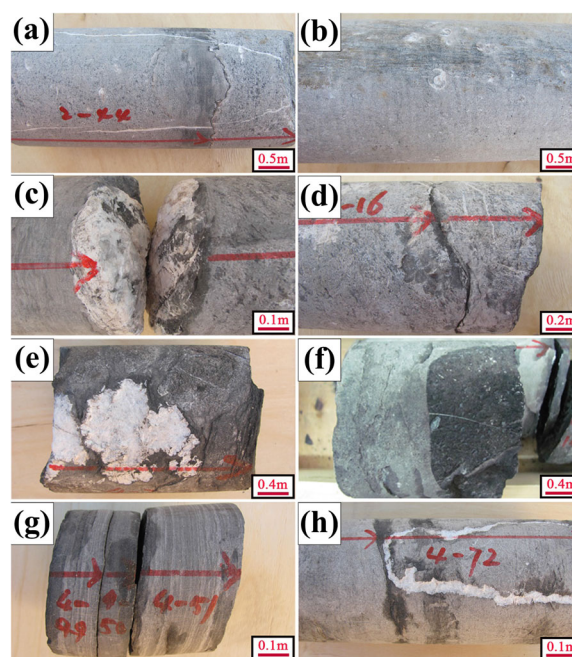


Figure 4. Observations of carbonate surfaces: (a) 2340.23–2343.85 m, limestone, cryptocrystalline structure, fracture, suture. (b) 2340.23–2343.85 m, limestone, cryptocrystalline structure, paleontological fossils. (c) 2497.30–2498.16 m, dolomitic limestone, cryptocrystalline structure, karst cave fully filled with calcite. (d) 2499.56–2501.00 m, siliceous limestone, silty structure, suture. (e) 2600.42–2603.60 m, limestone, argillaceous structure, middle hole fully filled with gypsum. (f) 2600.42–2603.60 m, limestone, argillaceous structure, middle hole fully filled with argillaceous. (g) 2604.55–2605.08 m, argillaceous limestone, argillaceous crystal structure, horizontal bedding. (h) 2607.63–2608.50 m, bioclastic limestone, bioclastic structure, oblique fracture, gypsum full filling.

oblique fractures and one fracture that is fully filled with gypsum.

Pore Characteristics Derived from Cast Thin Sections

After analyzing the cast thin section information for the 226 rock samples, it was concluded that the lithology in this area comprises mainly fine-grained limestone, bioclastic limestone and silty limestone. Moreover, the lithology contains a small amount of micritic limestone, sandy limestone, dolomitic limestone and calcareous dolomite (Fig. 5).

The reservoir space types of the Carboniferous carbonate reservoir in this area are complex and diverse. The primary pores were mainly biological cavities (Fig. 5e, g, j and k). The pore size was approximately 10–60 μm , with different sizes and

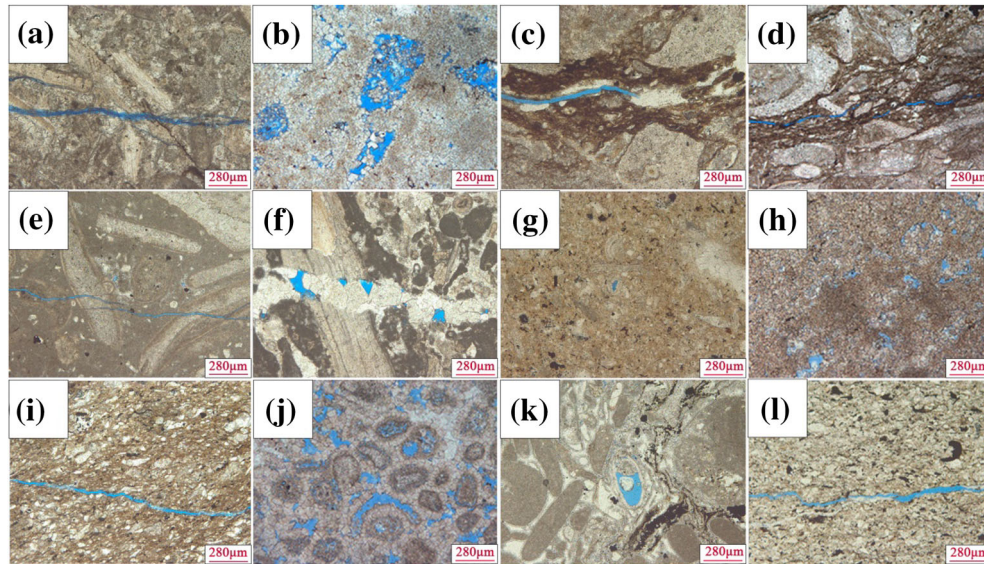


Figure 5. Cast thin section images: (a) K5, 2015-00,214, 1681.2 m, gray fine-grained limestone, microcracks. (b) K6, 2015-03,352, 1522.85 m, gray fine-grained limestone, solution pore. (c) K5, 2015-00,230, 1687.5 m, gray bioclastic limestone, semifilled joints. (d) K6, 2015-03,402, 1720.61 m, dark-gray bioclastic limestone, structural fracture. (e) K5, 2015-00,255, 1733.7 m, gray dolomitic silty limestone, microcracks, cavity holes. (f) P18, 2015-00,189, 1574.8 m, dark-gray silty limestone, semifilled joints. (g) A2, 2015-00,271, 2326.55 m, dark-gray silty limestone, body cavity hole. (h) K6, 2015-03,350, 1522.2 m, gray silty limestone, solution pore. (i) K5, 2015-00,204, 1678.7 m, dark-gray micrite limestone, microcracks. (j) K6, 2015-03,362, 1524.25 m, gray sandy limestone, solution pore, body cavity pore. (k) K5, 2015-00,248, 1730.15 m, gray dolomitic limestone, cavity hole. (l) K5, 2015-00,259, 1734.8 m, dark-gray calcareous dolomite, microcracks.

irregular shapes. The primary pore diameter was small, containing mostly isolated individuals, with poor connectivity and weak seepage capacity. The secondary pore spaces, such as solution pores and fractures, are the main reservoir spaces in this area. The secondary solution pores in this area were mainly intergranular solution pores, intragranular solution pores (Fig. 5b, h and j), and microfractures (Fig. 5a, e, i and l), with pore diameter of approximately 30–80 μm . Structural fractures are relatively developed in this area (Fig. 5d), which can increase its permeability. However, some structural fractures are filled with calcite (Fig. 5c and f), destroying the effectiveness of fractures and reducing permeability.

For gray fine-grained limestone, the bioclastic in the rock was mainly echinoderms and brachiopods. The matrix was mainly argillaceous calcite, partially cemented by bright calcite. Terrigenous clasts comprised silty quartz and feldspar, which mainly developed microcracks and intergranular dissolved pores (Fig. 5a and b). For gray bioclastic limestone, the organic argillaceous matter in the rock was distributed in a laminar form, and the terrigenous debris comprised rock debris and silty quartz and feldspar. The bioclastic was

dominated by echinoderms, which mainly developed semifilled fractures and structural fractures (Fig. 5c and d). The calcite in the silty limestone was in the shape of euhedral grains, and the gypsum was distributed in a porphyritic and uneven manner, which mainly developed solution pores, microcracks, body cavity pores, and semifilled joints (Fig. 5e, f, g and h). In the sandy limestone, the sandy debris in the rock was nearly round or short strips and the composition was argillaceous calcite. The particle size was mostly 0.125–0.25 mm. The sand debris was composed of powdery calcite and a small amount of gypsum, which mainly developed intergranular dissolved pores and body cavity pores (Fig. 5j). The average homogenization coefficient for the 12 samples was 0.64, the average pore diameter was 42.06 μm , and the average sorting coefficient was 20.49.

Pore Characteristics Derived from SEM Images

SEM images of varying magnification showed that the rock structure was generally dense and the connectivity was poor (Fig. 6). There were mainly

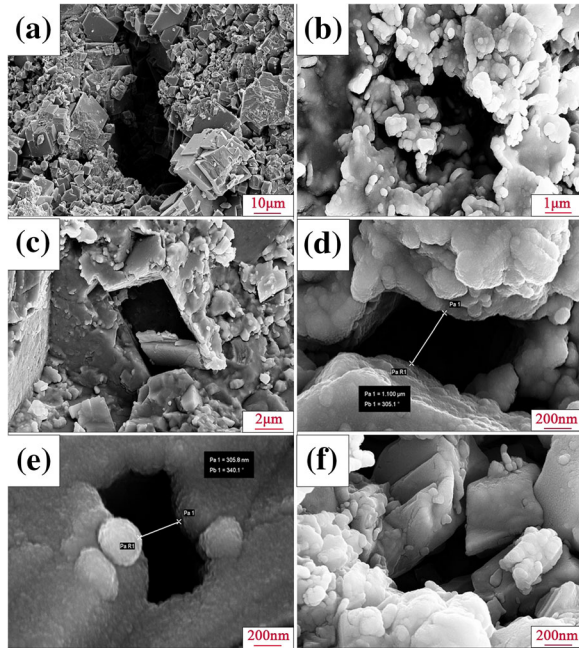


Figure 6. SEM images: (a) K6, 2015-03,362, 1524.25, gray arenaceous limestone, intergranular solution pores in the matrix. (b) K6, 2015-03,366, 1526.9, gray silty limestone, dissolved pores in the matrix. (c) K6, 2015-03,379, 1530.95, gray silty limestone, intergranular solution pore. (d) K6, 2015-03,393, 1535.95, dark gray marl, micron matrix solution pore. (e) K6, 2015-03,420, 1727.05, gray silty limestone, nanocrystalline intracrystalline solution pore. (f) T6, 2015-03,234, 2608.1, dark gray fine-grained limestone, intercrystalline pore.

euhedral calcite grains in the rock, with developed pores, intergranular pores, and intergranular dissolved pores with good connectivity (Fig. 6). As shown in Figure 6b, c, and f, the pores were not developed, dissolved pores and intergranular dissolved pores in the matrix were found, and the connectivity was poor. As shown in Figure 6d, the intergranular dissolved pores and micron matrix dissolved pores were in the matrix, and the size of the dissolved pores was approximately 1.1 μm with poor connectivity. As shown in Figure 6e, the pores were not developed. Dissolved pores and nanodissolved pores were found in the matrix, the size of the pores was approximately 305.8 nm, and the connectivity was poor.

The specific morphology of various minerals in the rock samples can be observed in the SEM images under different magnifications. Rock sample particles mainly comprised calcite grains (Fig. 7). Euhedral calcite grains were mainly seen in the rock, and irregular illite/smectite mixed-layer

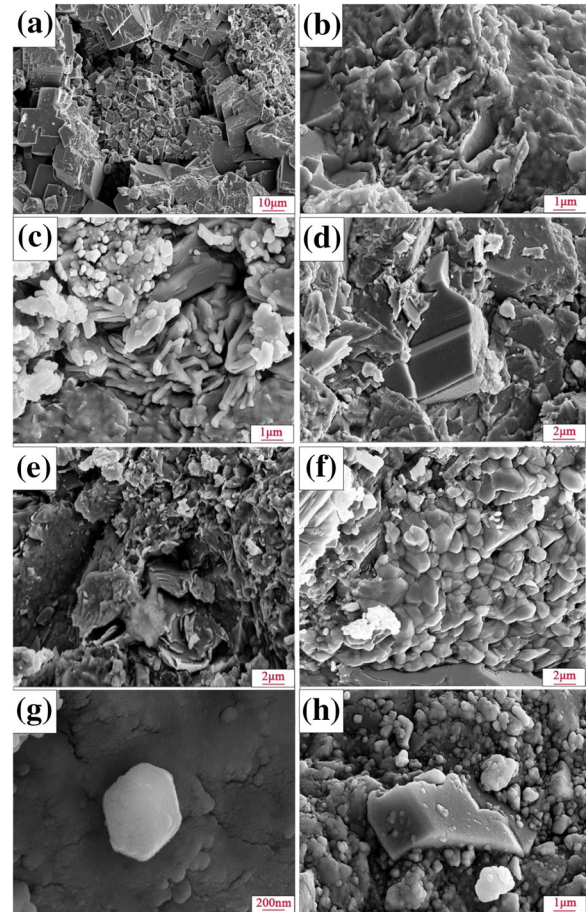


Figure 7. SEM images: (a) K6, 2015-03,362, 1524.25, gray arenaceous limestone, fine calcite grains between calcite crystals. (b) K6, 2015-03,366, 1526.9, gray silty limestone, irregular illite/smectite mixed-layer minerals. (c) K6, 2015-03,366, 1526.9, gypsum aggregate in the matrix. (d) K6, 2015-03,379, 1530.95, gray silty limestone, zeolite minerals in the matrix. (e) K6, 2015-03,420, 1727.05, gray silty limestone, irregular flake chlorite in the matrix. (f) T1, 2015-03,258, 3167.9, black gray micrite limestone, quartz aggregate in the matrix. (g) T1, 2015-03,255, 3166.5, gray micrite limestone, pyrite particles. (h) T6, 2015-03,234, 2608.1, dark-gray fine crystalline limestone, feldspar clasts in the matrix.

(Fig. 7b) and irregular flake chlorite (Fig. 7e) were distributed in the rock matrix. Moreover, gypsum aggregates (Fig. 7c), zeolite minerals (Fig. 7d), and quartz aggregates (Fig. 7f) were distributed in the matrix. Figure 7g shows how pyrite particles were distributed in the matrix. Figure 7h shows feldspar fragments in the matrix.

Table 1. Pore structure parameters obtained from capillary pressure curves of 18 samples

Well	Sample ID	Depth (m)	Strata	Pore volume (cm ³)	Sorting coefficient	Skewness	Capillary pressure (MPa)	Saturation median pressure (MPa)	Maximum pore throat radius (μm)	Average pore throat radius (μm)	Uniformity coefficient	
K6	2015-0.52	9.44	2.52	0.19		03,353	1523.35	C ₁ sr	2.29	1.93	0.72	0.08
K6	2015-0.49	13.30	3.20	0.16		03,362	1524.25	C ₁ sr	2.00	2.40	0.63	0.06
K6	2015-0.96	4.73	1.43	0.22		03,364	1525.05	C ₁ sr	2.16	2.11	0.56	0.16
K5	2015-146.2	1.22	0.23	0.07		00,214	1681.20	C ₁ sr	0.11	3.13	0.38	0.60
A2	2015-133.3	0.87	0.15	0.06		00,319	2338.42	C ₁ sr	0.11	2.85	0.30	0.84
A2	2015-56.3	1.19	0.26	0.09		00,322	2339.15	C ₁ sr	0.12	2.97	0.30	0.62
A2	2015-126.6	0.64	0.14	0.10		00,324	2339.72	C ₁ sr	0.07	2.91	0.65	1.15
A2	2015-100.8	0.31	0.08	0.14		00,336	2342.65	C ₁ sr	0.09	2.60	0.76	2.34
K5	2015-0.16	0.04	0.10			00,230	1687.50	C ₁ sr	0.29	2.35	0.78	4.51
K5	2015-147.8	0.29	0.06	0.09		00,248	1730.15	C ₁ v	0.24	2.47	0.50	2.49
K5	2015-84.41	0.52	0.11	0.09		00,255	1733.70	C ₁ v	0.60	2.53	0.22	1.41
K5	2015-159.9	0.63	0.14	0.10		00,259	1734.80	C ₁ v	0.35	2.94	0.51	1.17
K5	2015-129.7	0.61	0.12	0.08		00,237	1690.05	C ₁ v	0.67	2.70	0.28	1.20
K6	2015-0.42	0.08	0.12			03,426	1729.45	C ₁ v	0.30	1.14	-2.25	1.73
K6	2015-0.46	0.10	0.13			03,429	1793.70	C ₁ v	0.30	1.20	-1.99	1.59
K6	2015-15.34	0.88	0.17	0.11		03,350	1522.20	C ₁ v	1.22	1.46	-1.64	0.83
K6	2015-16.08	0.79	0.16	0.12		03,432	1795.40	C ₁ v	0.79	1.45	-1.54	0.93
K6	2015-18.35	0.60	0.15	0.16		03,436	1796.65	C ₁ v	0.77	1.38	-1.17	1.23

Pore Throat Characteristics Obtained by HPMT

Many parameters that reflect pore structure were obtained through the analysis of capillary pressure curves of 18 samples (Table 1). These 18 samples were divided into three types according to different curve shapes (Fig. 8a, c and e). The coexistence of three types of curves indicates very strong reservoir heterogeneity. The middle gentle section of the type I curve was very long, indicating a very concentrated distribution of rock pore channels, and a good sorting. The displacement pressure was less than 0.1 MPa, indicating that the rock had good

permeability, large pore radius, and good physical properties (Fig. 8a). Moreover, the pore throat radius corresponding to the type I curve was distributed mainly within 0.1–10 μm. Based on the Xoath classification criteria (Xoath, 1966), it was a mesopore, which is larger than the pore throat radius corresponding to type II and type III curves (Fig. 8b, d and f). The shape of the type II curve was similar to that of the type III curves. However, the saturation median pressure of the former was greater than 100 MPa (Fig. 8b), whereas that of the latter was less than 20 MPa (Fig. 8c). This indicates that the porosity and permeability characteristics of

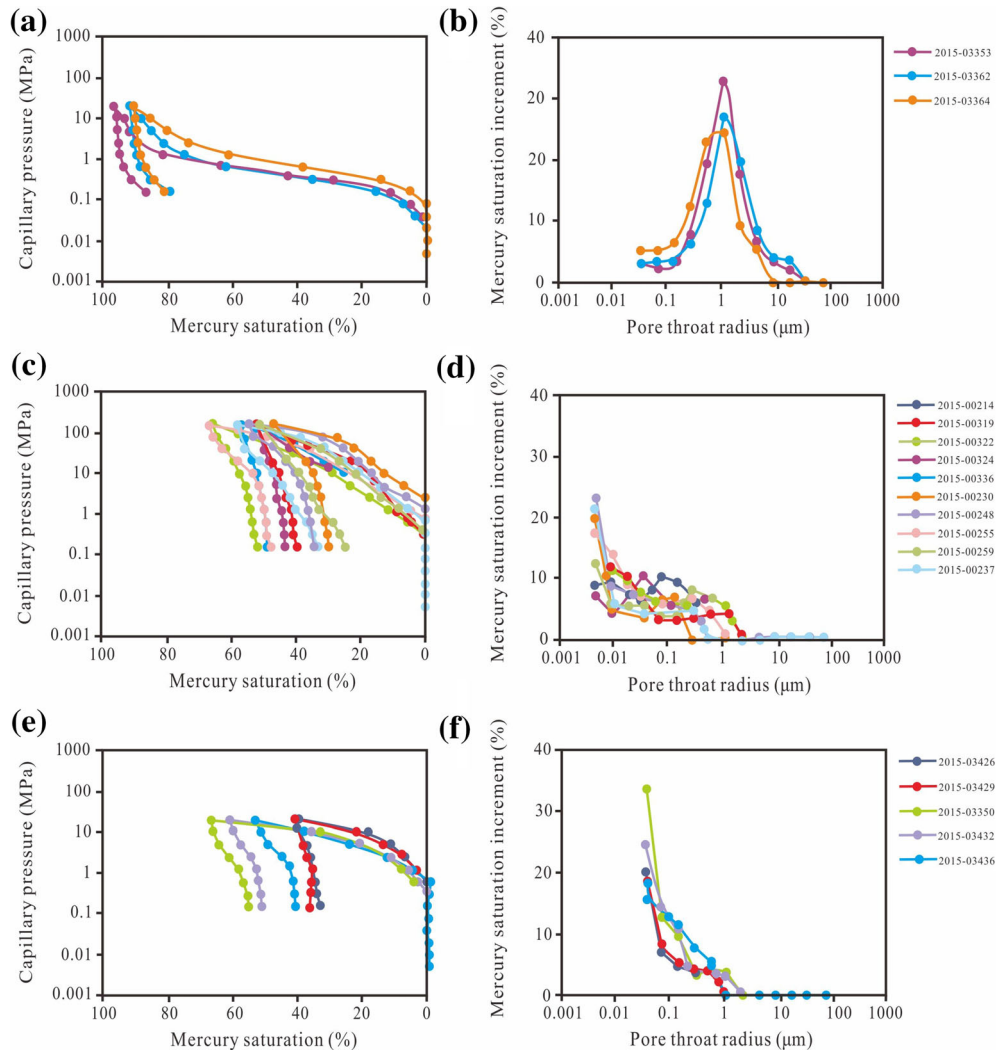


Figure 8. HPMI curves (a, c and e) and corresponding pore throat radius distributions (b, d, and f) of the three types of samples.

the type III curve were better than those of the type II curve. The displacement pressure of type II and type III curves was approximately 1 MPa, which was greater than that of the type I curve. This indicates that the physical properties of type II and type III curves were worse than those of the type I curve. This is consistent with the porosity and permeability results measured via conventional physics shown in Figure 3.

The greater the throat uniformity coefficient of a reservoir rock, the greater the throat radius of its constituent rock. Therefore, the closer it is to the maximum radius of reservoir throat, the more uniform is the reservoir throat. The average uniformity coefficient of the type I curve was 0.19, which was

greater than that of types II and III curves, indicating that its throat radius was the largest. A sorting coefficient close to 1.0 indicates that the pore network is well sorted. The higher the sorting coefficient, the worse is the uniformity of the pore network (Li et al., 2017). As presented in Table 1, the sorting coefficient of the type II curve was the largest, with average of 2.745, indicating that the sorting of the reservoir pore network was the worst. Table 1 presents that the skewness of the type I curve was 0.56–0.72 (average 0.64), which was greater than that of types II and III curves. This indicates that the reservoir corresponding to the type I curve was mainly of macroporous throat. Therefore, based on the shape of capillary pressure

Table 2. Evaluation parameters of fractal dimension of the core pore structure

Well	Sample ID	Depth (m)	Strata	Porosity (%)	Permeability (mD)	D_1	R_1^2	D_2	R_2^2	D_3	R_3^2	D
K6	2015-03,353	1523.35	C ₁ sr	20.80	18.800	2.4097	0.9574	2.9277	0.9612	2.3488	0.9738	2.6833
K6	2015-03,362	1524.25	C ₁ sr	17.20	14.000	2.5666	0.9746	2.9022	0.9513	2.5839	0.9908	2.5732
K6	2015-03,364	1525.05	C ₁ sr	18.90	1.900	2.5028	0.9898	-	-	-	-	-
K5	2015-00,214	1681.20	C ₁ sr	1.00	0.025	2.8866	0.9450	-	-	-	-	-
A2	2015-00,319	2338.42	C ₁ sr	1.00	1.810	2.8778	0.8769	-	-	-	-	-
A2	2015-00,322	2339.15	C ₁ sr	1.10	0.854	2.8262	0.9313	-	-	-	-	-
A2	2015-00,324	2339.72	C ₁ sr	0.60	0.017	2.8550	0.9877	-	-	-	-	-
A2	2015-00,336	2342.65	C ₁ sr	0.8	0.075	2.8199	0.9870	-	-	-	-	-
K5	2015-00,230	1687.50	C ₁ sr	2.90	0.109	2.8586	0.8357	-	-	-	-	-
K5	2015-00,248	1730.15	C ₁ v	2.10	0.123	2.8553	0.8007	-	-	-	-	-
K5	2015-00,255	1733.70	C ₁ v	5.20	6.470	2.8088	0.8487	-	-	-	-	-
K5	2015-00,259	1734.80	C ₁ v	4.00	2.280	2.8824	0.9359	-	-	-	-	-
K5	2015-00,237	1690.05	C ₁ v	6.20	2.600	2.8585	0.8200	-	-	-	-	-
K6	2015-03,426	1729.45	C ₁ v	2.50	0.024	2.8499	0.8180	-	-	-	-	-
K6	2015-03,429	1793.70	C ₁ v	2.70	0.245	2.8384	0.8653	-	-	-	-	-
K6	2015-03,350	1522.20	C ₁ v	10.20	0.274	2.7376	0.7290	-	-	-	-	-
K6	2015-03,432	1795.40	C ₁ v	7.10	0.037	2.7638	0.8127	-	-	-	-	-
K6	2015-03,436	1796.65	C ₁ v	6.80	0.036	2.7482	0.9516	-	-	-	-	-

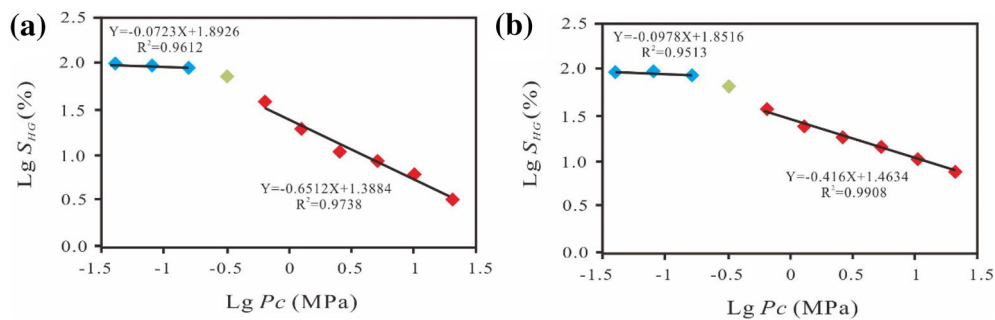


Figure 9. Fractal dimension obtained by piecewise linear fitting trend line for (a) sample 2015-03,353, and (b) sample 2015-03,362. (blue plots represent coarse pore throat, green plots represent transition pore throat, and red plots represent fine pore throat).

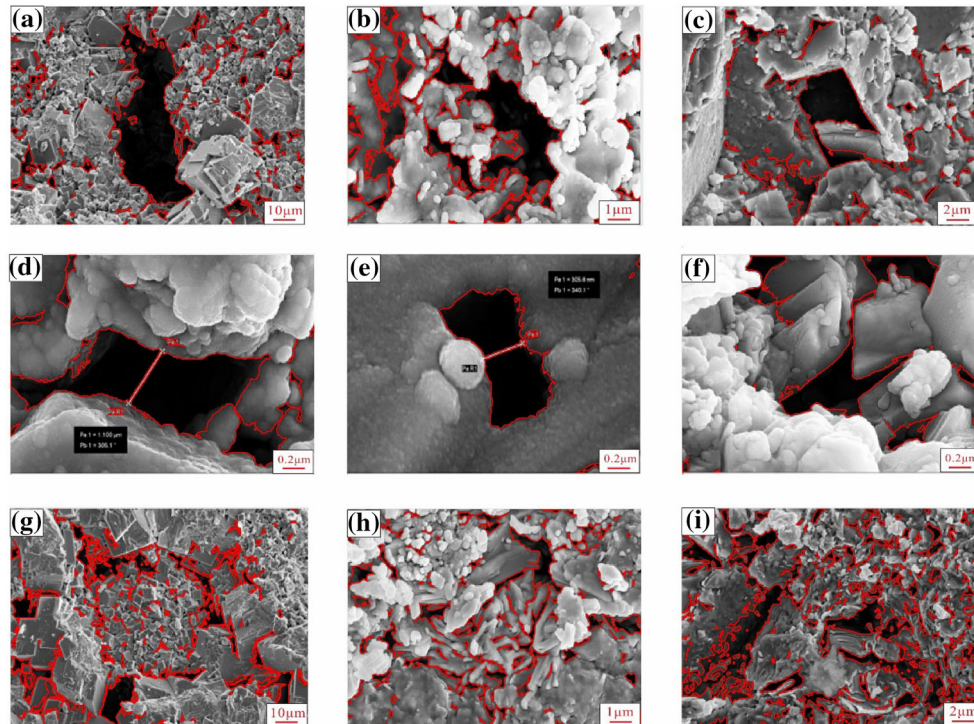


Figure 10. Pore distribution extracted by JMicroVision software. (a) K6, 2015-03,362. (b) K6, 2015-03,366. (c) K6, 2015-03,379. (d) K6, 2015-03,393. (e) K6, 2015-03,420. (f) T6, 2015-03,234. (g) K6, 2015-03,362. (h) K6, 2015-03,366. (i) K6, 2015-03,420.

curve and relevant parameters, it can be concluded that the types I, II, and III curves represent the best, worst, and intermediate rock physical properties, respectively.

Fractal Dimension Obtained from HPMI

Using the mercury injection data presented in Table 1, a scatter diagram was created on the double logarithm coordinate system of $\lg P_c - \lg S_w$ to obtain the piecewise linear fitting trend line and the overall linear fitting trend line. Equations 5 and 6 were used to calculate fractal dimension (Table 2). The slope of a straight line fitted by all logarithmic scatter points was used to calculate the overall linear regression fractal dimension D_1 . Piecewise linear regression fractal dimension D was fitted piecewise according to the shape of scatter plot curve. Two samples (2015-03,353 and 2015-03,362) located in a high-porosity and high-permeability zone showed piecewise linear fitting trend lines and that D_2 was larger than D_3 of the fine pore throat (Fig. 9), indicating a complex pore structure of the coarse pore

throat. As presented in Table 2, little difference was found between a fractal dimension obtained by fitting an overall linear regression and by piecewise fitting a linear regression; however, the curve fitted by the latter is more realistic, and the calculated fractal dimension were more accurate. Therefore, the piecewise linear regression fractal dimensions were used for subsequent experiments. The fractal dimensions of all samples ranged from 2.5028 to 2.8866. The fractal dimensions of samples 2015-03,353, 2015-03,362, and 2015-03,364 that correspond to a type I curve were 2.5028–2.6833, with average of 2.5864, which was the lowest among the samples. This indicates that the pore network is not complex, consistent with the results obtained using the mercury injection curves.

Fractal Dimension Obtained from SEM

Some SEM images in Figures 6 and 7 are used to extract the identified pore equivalent perimeter and area (Fig. 10) in the JMicroVision image analysis software. The pore structure parameters were

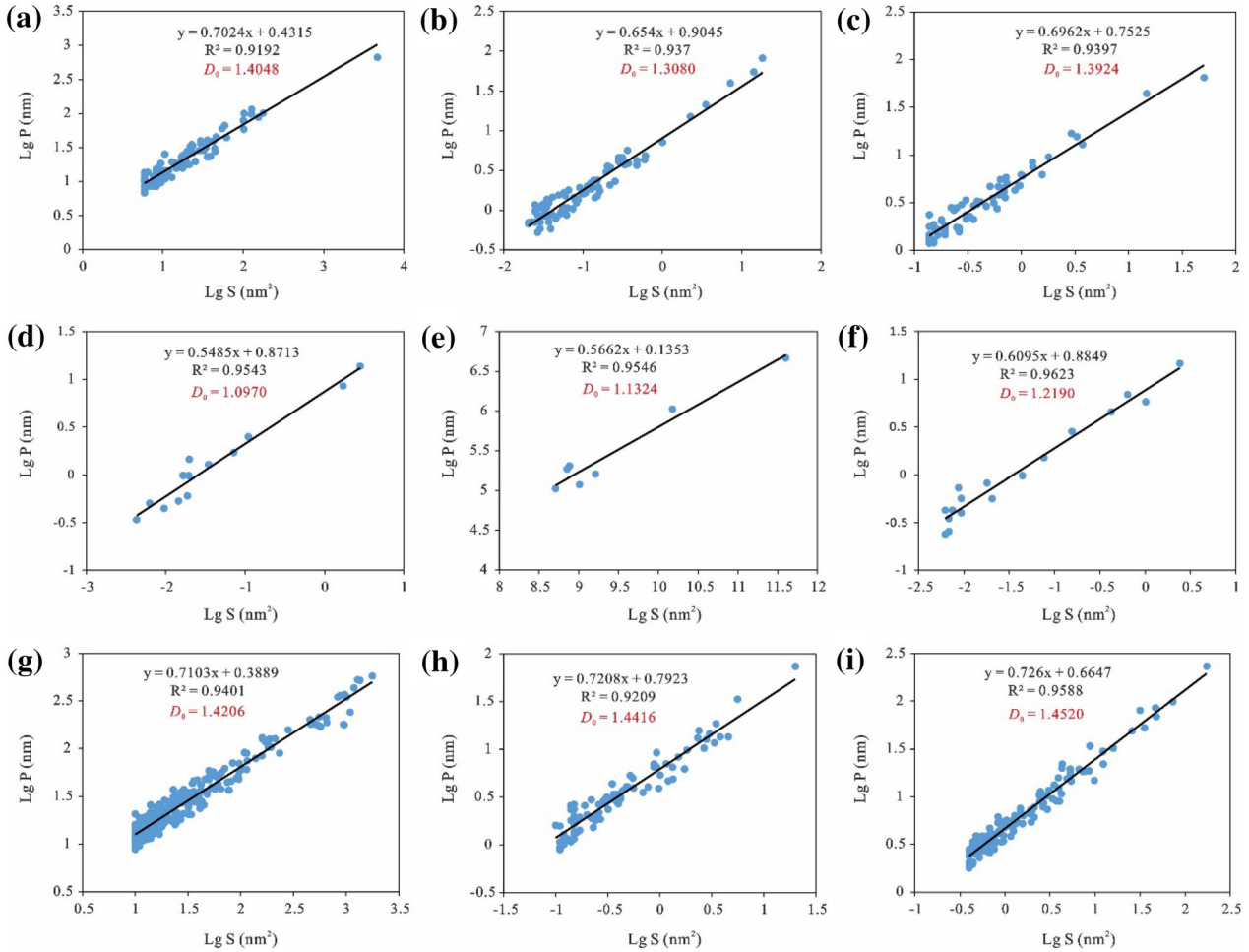


Figure 11. Fractal relationships between pore perimeter and area calculated based on high-resolution scanning electron microscope photos. (a) K6, 2015-03,362. (b) K6, 2015-03,366. (c) K6, 2015-03,379. (d) K6, 2015-03,393. (e) K6, 2015-03,420. (f) T6, 2015-03,234. (g) K6, 2015-03,362. (h) K6, 2015-03,366. (i) K6, 2015-03,420.

plotted in double logarithmic coordinates (Fig. 11). Straight lines were obtained through least square fitting. Fractal dimensions of different pore types were calculated using the slope of the straight lines. The closer D_0 is to 1, the smaller is the heterogeneity. The calculation results show (Fig. 11) that the fractal dimensions D_0 varied between 1.0970 and 1.4520, with average of 1.3186, and the correlation coefficient varied between 0.9192 and 0.9623, indicating strong porosity heterogeneity of carbonate rocks in this area, with significant fractal characteristics.

Fracture Characteristics and Occurrence Statistics

After observing the imaging logging image, it was determined that the fractures in well A2 included conductivity fractures, fissures, and resistive fractures (Fig. 12). Conductivity fractures are natural fractures that are crucial in determining reservoir characteristics and oil and gas migration. The FMI image showed a dark sinusoidal curve (Fig. 13) caused by drilling mud invasion or argillaceous and conductive mineral filling. Few conductivity fractures were found in the carbonate section of the well, which were mainly developed in gypsum limestone and argillaceous limestone. The conductivity fractures trend mainly NW–SE and near E–W, with inclinations of 16° – 76° (Fig. 12). The effectiveness of some conductivity fractures was poor

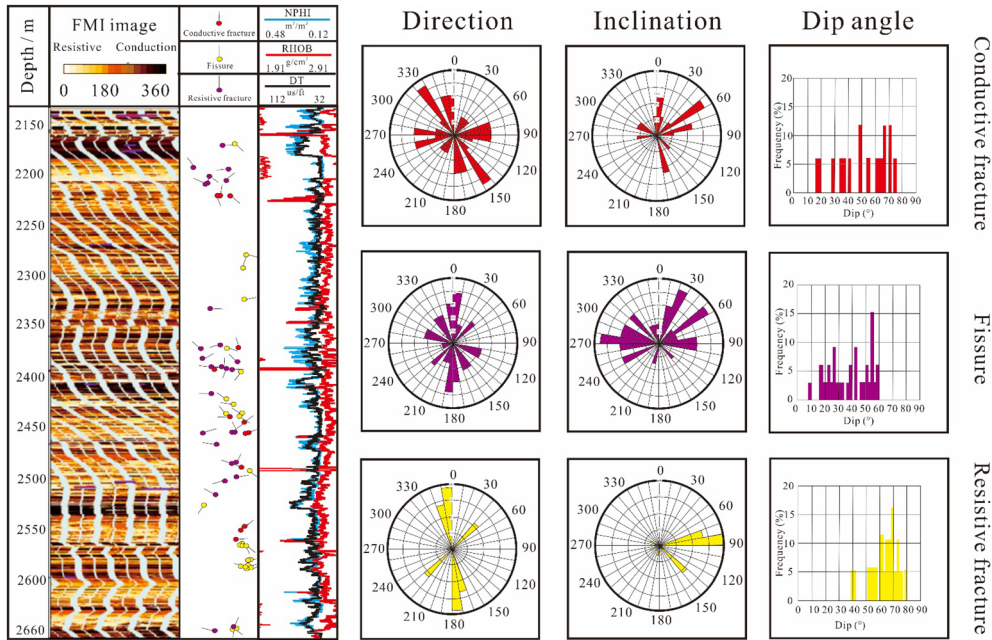


Figure 12. Occurrence characteristics of fractures in the whole section of well A2.

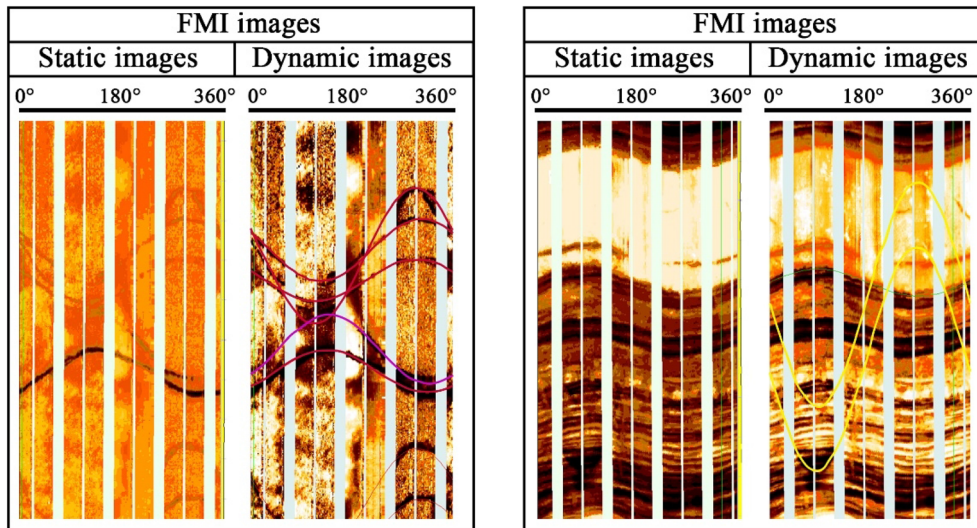


Figure 13. FMI image characteristics of fractures in well A2. High-conductivity fracture, red; Micro-fissure, purple; High-resistance fracture, yellow.

because they were partially filled with calcite or gypsum.

Fissures are also a type of conductivity fracture, including condensation shrinkage fractures, joint fractures, and intergravel fractures, which can

effectively improve the porosity and permeability of a reservoir. Fissures refer to conductivity fractures that are difficult to fit theoretically on a FMI image. They are characterized by a dark color in FMI images. Some fissures were very short, some had a

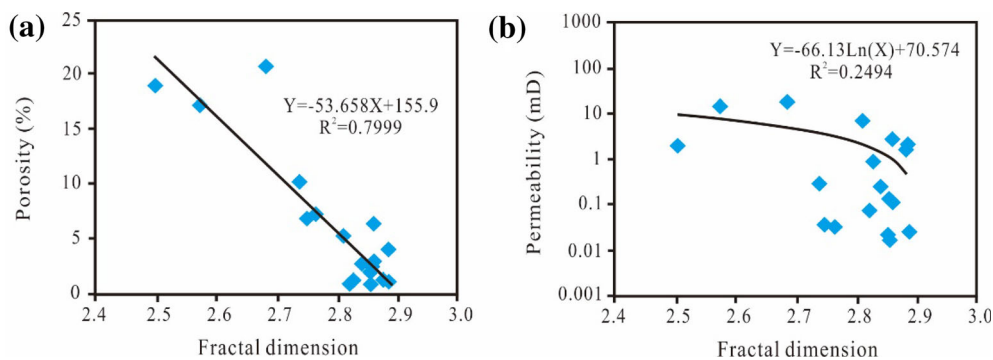


Figure 14. (a) Correlation of fractal dimension with porosity. (b) Correlation of fractal dimension with permeability.

high angle or large length, and some were characterized by partial sinusoidal curves (Fig. 13). In this study, partial sinusoidal curves were used to obtain the occurrence characteristics of fissures. Fissures were mainly developed in gypsum, gypsum limestone, and argillaceous limestone, striking nearly N–S and NW–SE with medium–low angles of 9° – 60° (Fig. 12).

Resistive fractures are formed by filling with high-resistivity materials or fracture closure and do not contribute to a reservoir. In the FMI image (Fig. 13), resistive fractures exhibit a relatively high-resistance (light color to white) sinusoidal curve, which is formed by the filling of high-resistance material or the closure of the fracture. Resistive fractures of the well mainly strike nearly N–S and NE–SW, with angles of 40° – 80° . They are mainly developed in C_{1V2} limestone and C_{1V3} argillaceous limestone (Fig. 12).

DISCUSSION

Influence Factors of Fractal Dimension

Porosity and Permeability

The correlations among porosity, permeability, and fractal dimension were drawn to study the relationships among them (Fig. 14). The fractal dimension gradually approached 3 with decrease in porosity and permeability; that is, the complexity of pore network became increasingly high. A strong negative correlation was observed between pore throat fractal dimension and porosity (Fig. 14), and the correlation coefficient was -0.7999 . Porosity

reflects the proportion of pore space volume in a rock. Generally, the complexity of pore distribution does not affect the porosity of conventional reservoirs (Shao et al., 2017). However, a previous study found that the irregular distribution of fine pore throats in tight reservoirs may inhibit large pores (Chalmers and Bustin, 2008). A negative but weak correlation was observed between permeability and fractal dimension (Fig. 14b). A large fractal dimension indicates change in pore shape from regular to complex, which will hinder fluid flow and reduce permeability accordingly. However, the correlation may not be particularly obvious as there are several fractures in carbonate reservoirs in this area (Wei et al., 2019).

In conclusion, a good correlation exists between fractal dimension and the physical properties of the reservoir. Therefore, in the study area, the pore throat fractal dimension can be used to characterize the complexity of reservoir micropore structures. The larger the pore throat fractal dimension, the more complex the reservoir micropore structure.

Pore Structure Parameters

The effect of pore structure parameters on fractal dimension was studied in this work (Fig. 15). The fractal dimension was correlated positively with displacement pressure and saturation median pressure, with correlation coefficients of 0.5936 and 0.3622, respectively (Fig. 15). The pore structure becomes complex with increasing fractal dimension, and it is relatively more difficult for mercury to enter the pore throat network system. Consequently, displacement pressure and saturation median pressure

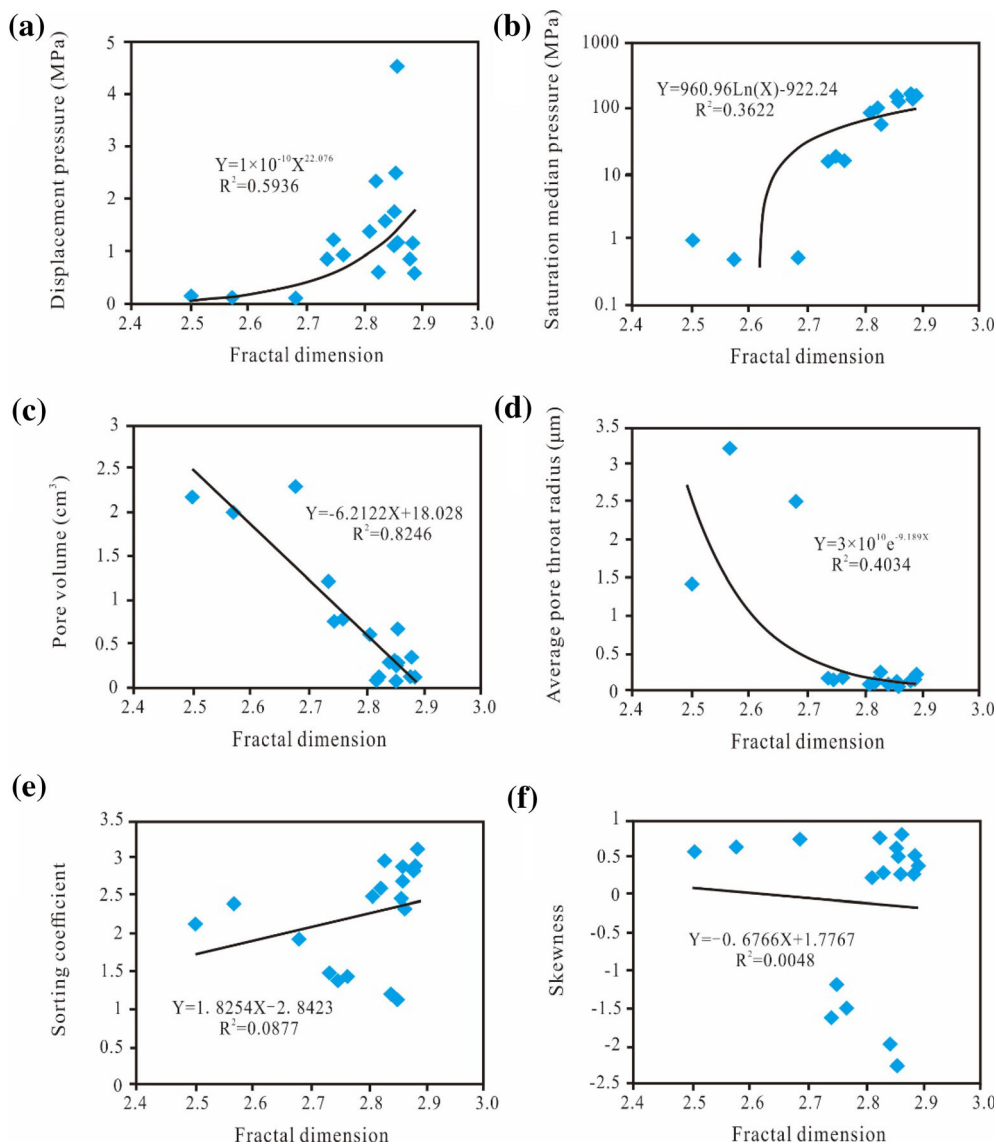


Figure 15. Correlation between fractal dimension and pore structure parameters. (a) Displacement pressure. (b) Saturation median pressure. (c) Pore volume. (d) Average pore throat radius. (e) Sorting coefficient. (f) Skewness.

also increase. It was observed that fractal dimension had strong negative correlations with pore volume and average pore throat radius, with correlation coefficients of -0.8246 and -0.4034 , respectively. These parameters decrease gradually with increasing fractal dimension. The correlation of fractal dimension with sorting coefficient and skewness was poor, with correlation coefficients of 0.0877 and 0.0048 , respectively. This indicates that fractal dimension has a little effect on reservoir pore throat sorting. The foregoing results show that fractal dimension can well characterize the heterogeneity of pores.

Causes of High-Porosity and High-Permeability Zones

As discussed in Section “Conventional Petrophysical Measurements”, although most samples were very dense, the maximum porosity and permeability reached 20.8% and 18.8 mD, respectively, in well K6 with depth of 1522.85 – 1525.05 m (Fig. 3a). Moreover, the pore types in this interval were mainly intergranular dissolved pores, intra-granular dissolved pores, and microfractures, which were well developed (Fig. 5b and j). There were

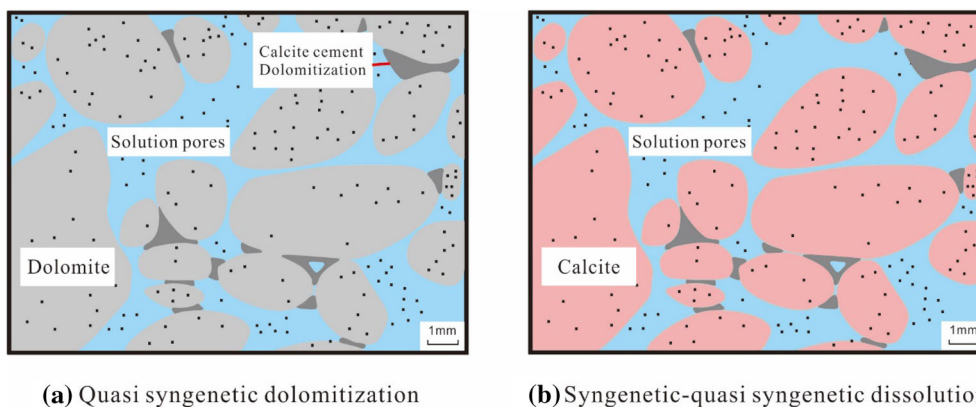


Figure 16. Evolution model of the Lower Carboniferous granular beach dolomite vuggy reservoir (modified from Zhou et al., 2015).

mainly euhedral calcite grains in the rock, with developed pores, intergranular pores, and intergranular dissolved pores. Good connectivity was also noted (Fig. 6a). The distribution of rock pores and channels in this depth section was very concentrated and had good sorting (Fig. 8a and b). This is closely associated with the sedimentary environment and diagenesis.

In the process of reservoir deposition in this section, the sedimentary environment changed from an open platform to an evaporation platform (Fig. 1c), and dolomite was associated with high micritic dolomite and gypsum content, characterized by an evaporation environment. This was conducive to quasi-syngenetic dolomitization (Fig. 16a). In addition, the maximum content of iron dolomite in the reservoir of this section can reach 98.17% (Fig. 2a). The dolomite crystal was very small, resulting from the rapid crystallization of dolomitization in the quasi-syngenetic stage. It can thus be inferred that the pore network was transformed by dolomitization (Sun et al., 2005; Li and Li, 2019; Pei et al., 2021). Under an overall arid climate background, when there is atmospheric fresh water supply, aragonitic particles or cements dissolve to produce holes and release a large amount of Mg^{2+} , providing a source of Mg^{2+} for quasi-syngenetic dolomitization. In an arid and hot climate, the surface seawater or pore water is concentrated and salted continuously due to strong evaporation, forming brine with high Mg^{2+}/Ca^{2+} values, leading to dolomitization of the surrounding sediments. When excess brine permeates downward, dolomitization of sediments passing by with high-porosity and high-permeability occurs (Zhou et al., 2015). Usually,

after dolomitization, the crystal volume of calcite decreases, which will produce secondary pores and increase porosity. Microscopically, biological cavity pores, intergranular dissolution pores, intragranular dissolution pores, and microfractures were developed in this interval (Fig. 5); however, most of the pores formed by dissolution in this period were filled by later cementation filling, indicating that they were formed early. Therefore, it is speculated that dissolution in this period occurred in a syngenetic–quasi-syngenetic period (Fig. 16b) (Meng et al., 2015). In this sedimentary stage, the decline of sea level caused the shallowing of water bodies. The beach facies, such as the granular beach and Tainei beach developed in this section, were exposed to the sea. In an atmospheric fresh water environment, unstable minerals, such as aragonite and high-magnesium calcite, are dissolved to form selective pores and fractures. Quasi-syngenetic dissolution and quasi-syngenetic dolomitization complement each other. During long geological evolution, and owing to periodic changes in climate and sea level rise and fall, dissolution and dolomitization occur alternately or dissolution occurs mainly in one period and dolomitization in another, resulting in holes and sediments being transformed into dolomite. After diagenetic evolution of this stage, the pore type changed from original intergranular pores to solution pores and karst caves, supplemented by intergranular pores. Therefore, quasi-syngenetic dolomitization and syngenetic–quasi-syngenetic dissolution had greatly improved the physical properties of the reservoir and promoted the formation of high-porosity and high-permeability zones.

CONCLUSIONS

In this study, various experimental means and related theories were used to evaluate comprehensively the pore structure of the Lower Carboniferous carbonate reservoirs in the Marsel exploration area of the Chu-Sarysu Basin and the following conclusions were drawn.

- (1) Based on cast thin section and SEM, it is concluded that the lithology in this area comprises mainly fine-grained limestone, bioclastic limestone, and silty limestone. The rock structure was generally dense, but it had some high-porosity and high-permeability zones. This was due mainly to the considerable improvement in the physical properties of the reservoir caused by quasi-syngenetic dolomitization and syngenetic–quasi-syngenetic dissolution. The primary pores were mainly biological cavities. The secondary dissolution pores were mainly dissolution pores and microfractures. Through observation of FMI images, the fractures of well A2 were identified, including conductivity fractures, fissures and resistive fractures. Structural fractures were relatively developed in this area, which can increase the percolation capacity of the reservoir. However, some structural fractures were filled with calcite, reducing the percolation capacity of the reservoir.
- (2) By analyzing the capillary pressure curve of the samples, they were divided into three types according to different curve forms. The rocks corresponding to type I curves in high-porosity and permeability zone had good sorting, good permeability, large pore radius, and good physical properties. The physical properties of the rock represented by type II curves were the worst, and those of type III curves were intermediate.
- (3) According to the mercury injection data, the average fractal dimension of the sample corresponding to type I curves was 2.5864, which was the lowest, indicating that the pore network was not complex. Two samples (2015-03,353 and 2015-03,362) located in the high-porosity and high-permeability zones showed piecewise linear fitting trend lines, indicating that the fractal dimension of coarse pore throats was larger than that of fine pore throats, and that the pore structure of coarse

pore throats was more complex. Overall, a good correlation exists between fractal dimension and physical properties of the reservoir. The larger the fractal dimension of the pore throats, the more complex the micropore structure of the reservoir.

ACKNOWLEDGMENTS

We thank the three anonymous reviewers for their valuable comments, who improved the study. This study was financially supported by the Joint Funds of National Natural Science Foundation of China (U19B6003-02), the CNPC Science and Technology Major Project of the Fourteenth Five-Year Plan (2021DJ0101), and the National Natural Science Foundation of China (42202133, 42102145).

DECLARATIONS

Conflict of Interest The authors declare that they have no known competing financial interests or personal relationships that could have appeared to influence the work reported in this paper.

REFERENCES

- Aghli, G., Moussavi-Harami, R., & Mohammadian, R. (2018). Reservoir heterogeneity and fracture parameter determination using electrical image logs and petrophysical data (a case study, carbonate Asmari Formation, Zagros Basin, SW Iran). *Petroleum Science*, 17(1), 19.
- Brandano, M., & Civitelli, G. (2007). Non-seagrass meadow sedimentary facies of the Pontinian Islands, Tyrrhenian Sea: A modern example of mixed carbonate–siliciclastic sedimentation. *Sedimentary Geology*, 201(3), 286–301.
- Brunet, M. F., Volozh, Y. A., & Antipov, M. P. (1999). The geodynamic evolution of the Precaspian Basin Kazakhstan along a north–south section. *Tectonophysics*, 313(1–2), 85–106.
- Bykadorov, V. A., Bush, V. A., Fedorenko, O. A., Filippova, I. B., Miletenko, N. V., Puchkov, V. N., Smirnov, A. V., & Volozh, B. U. A. (2003). Ordovician–permian palaeogeography of central eurasia: Development of palaeozoic petroleum-bearing basins. *Journal of Petroleum Geology*, 26(3), 325–350.
- Chalmers, G. R., & Bustin, R. M. (2008). Lower Cretaceous gas shales in northeastern British Columbia, part I: Geological controls on methane sorption capacity. *Bulletin of Canadian Petroleum Geology*, 56(1), 1–21.
- Chang, J. Q., Fan, X. D., Jiang, Z. X., Wang, X. M., Chen, L., Li, J. T., Zhu, L., Wan, C. X., & Chen, Z. X. (2021). Differential impact of clay minerals and organic matter on pore structure and its fractal characteristics of marine and continental shales in China. *Apply Clay Science*, 216, 106334.

- Chen, L. P., Zhang, H., Cai, Z. X., Hao, F., Xue, Y. F., & Zhao, W. S. (2022). Petrographic, mineralogical and geochemical constraints on the fluid origin and multistage karstification of the middle-lower Ordovician carbonate reservoir, NW Tarim Basin, China. *Journal of Petroleum Science and Engineering*, 208, 109561.
- Cook, H. E., Zhemchuzhnikov, V. G., Zempolich, W. G., Lehmann P. J., & Zorin A. Y. (2007). Devonian and carboniferous carbonate platform facies in the Bolshoi Karatau, southern Kazakhstan: Outcrop analogs for coeval carbonate oil and gas fields in the north Caspian Basin. AAPG, New York. <https://doi.org/10.1306/1205837St55372>.
- Degiorgio, V., & Mandelbrot, B. B. (1984). The fractal geometry of nature. *Mathematical Association of America*, 91(9), 594.
- Dou, W. C., Liu, L. F., Wu, K. J., Xu, Z. J., Liu, X. X., & Feng, X. (2018). Diagenetic heterogeneity, pore throats characteristic and their effects on reservoir quality of the Upper Triassic tight sandstones of Yanchang Formation in Ordos Basin, China. *Marine and Petroleum Geology*, 98, 243–257.
- Fu, H. J., Tang, D. Z., Xu, T., Tao, S., Li, S., Yin, Z. Y., Chen, B. L., Zhang, C., & Wang, L. L. (2017). Characteristics of pore structure and fractal dimension of low-rank coal: A case study of Lower Jurassic Xishanyao coal in the southern Junggar Basin, NW China. *Fuel*, 193(1), 254–264.
- Haines, T. J., Michie, E., Neilson, J. E., & Healy, D. (2016). Permeability evolution across carbonate hosted normal fault zones. *Marine and Petroleum Geology*, 72, 62–82.
- Hamd, J., Cerepi, A., Swennen, R., Loisy, C., Galaup, S., & Pigot, L. (2022). Sedimentary and diagenetic effects on reservoir properties of Upper Cretaceous Ionian Basin and Kruja platform carbonates, Albania. *Marine and Petroleum Geology*, 138, 105549.
- Hassan, N. M., Yan, D. T., Nayima, H., Umar, A., & Riaz, H. R. (2020). Pore structure characteristics and fractal dimension analysis of low rank coal in the Lower Indus Basin, SE Pakistan. *Journal of Natural Gas Science and Engineering*, 77, 103231.
- He, J. H., Ding, W. L., Li, A., Sun, Y. X., Dai, P., Yin, S., Chen, E., & Gu, Y. (2016). Quantitative microporosity evaluation using mercury injection and digital image analysis in tight carbonate rocks: A case study from the Ordovician in the Tazhong Palaeouplift, Tarim Basin, NW China. *Journal of Natural Gas Science and Engineering*, 34, 627–644.
- Hu, T., Pang, X. Q., Jiang, F. J., & Zhang, C. X. (2022a). Dynamic continuous hydrocarbon accumulation (DCHA): Existing theories and a new unified accumulation model. *Earth-Science Reviews*, 232, 104109.
- Hu, T., Pang, X. Q., Xu, T. W., & Li, C. R. (2022b). Identifying the key source rocks in heterogeneous saline lacustrine shales: Paleogene shales in the Dongpu depression, Bohai Bay Basin, eastern China. *AAPG Bulletin*, 106(6), 1325–1356.
- Hu, Y. B., Guo, Y. H., Shangguan, J. W., Zhang, J. J., & Song, Y. (2020). Fractal characteristics and model applicability for pores in tight gas 2 sandstone reservoirs: A case study of the Upper Paleozoic in Ordos. *Energy and Fuels*, 34(12), 16059–16072.
- Jaireth, S., & Hustone, D. (2010). Metal endowment of cratons, terranes and districts: Insights from a quantitative analysis of regions with giant and super-giant deposits. *Ore Geology Reviews*, 38(3), 288–303.
- Jarvie, D. M., Hill, R. J., Ruble, T. E., & Pollastro, R. M. (2007). Unconventional shale-gas systems: The Mississippian Barnett Shale of north-central Texas as one model for thermogenic shale-gas assessment. *AAPG Bulletin*, 91(4), 475–499.
- Jiang, F., Chen, D., Chen, J., Li, Q., & Dai, J. (2016). Fractal analysis of shale pore structure of continental shale gas reservoir in the Ordos Basin, NW China. *Energy and Fuels*, 30(6), 4676–4689.
- Lai, J., Li, D., Wang, G. W., Xiao, C. W., Hao, X. L., Luo, Q. Y., Lai, L. B., & Qin, Z. Q. (2018a). Earth stress and reservoir quality evaluation in high and steep structure: The Lower Cretaceous in the Kuqa Depression, Tarim Basin, China. *Marine and Petroleum Geology*, 101, 43–54.
- Lai, J., & Wang, G. W. (2015). Fractal analysis of tight gas sandstones using high-pressure mercury intrusion techniques. *Journal of Natural Gas Science and Engineering*, 24, 185–196.
- Lai, J., Wang, G. W., Wang, S., Cao, J. T., Li, M., Pang, X. J., Han, C., Fan, X. Q., Yang, L., He, Z. B., & Qin, Z. Q. (2018b). A review on the applications of image logs in structural analysis and sedimentary characterization. *Marine and Petroleum Geology*, 95, 139–166.
- Li, C. Y., Dai, W. H., Luo, B. F., Pin, J., Liu, Y. S., & Zhang, Y. (2020a). New fractal-dimension-based relation model for estimating absolute permeability through capillary pressure curves. *Journal of Petroleum Science and Engineering*, 196, 107672.
- Li, K. W. (2010). Analytical derivation of Brooks-Corey type capillary pressure models using fractal geometry and evaluation of rock heterogeneity. *Journal of Petroleum Science and Engineering*, 73(1–2), 20–26.
- Li, P., Zheng, M., Bi, H., Wu, S. T., & Wang, X. R. (2017). Pore throat structure and fractal characteristics of tight oil sandstone: A case study in the Ordos Basin, China. *Journal of Petroleum Science and Engineering*, 149(20), 665–674.
- Li, Q. Y., & Li, Q. (2019). Diagenesis and its effects on the reservoir of Leikoupo formation in Longmendong area of Southwestern Sichuan. *Science Technology and Engineering*, 19(30), 103–112.
- Li, Q. W., Pang, X. Q., Li, B. Y., Zhao, Z. F., Shao, X. H., Zhang, X., Wang, Y. W., & Li, W. (2018). Discrimination of effective source rocks and evaluation of the hydrocarbon resource potential in Marsel, Kazakhstan. *Journal of Petroleum Science and Engineering*, 160, 194–206.
- Li, W. Q., Mu, L. X., Zhao, L., Li, J. X., Wang, S. Q., Fan, Z. F., Shao, D. L., Li, C. H., Shan, F. C., Zhao, W. Q., & Sun, M. (2020b). Pore-throat structure characteristics and their impact on the porosity and permeability relationship of Carboniferous carbonate reservoirs in eastern edge of Pre-Caspian Basin. *Petroleum Exploration and Development*, 47(5), 958–971.
- Liu, X. P., Lai, J., Fan, X. C., Shu, H. L., Wang, G. C., Ma, X. Q., Liu, M. C., Guan, M., & Luo, Y. F. (2020). Insights in the pore structure, fluid mobility and oiliness in oil shales of Paleogene Funing Formation in Subei Basin, China. *Marine and Petroleum Geology*, 114, 104228.
- Mandelbrot, B. B. (1975). Stochastic models for the Earth's relief, the shape and the fractal dimension of the coastlines, and the number-area rule for islands. *Proceedings of the National Academy of Sciences*, 72(10), 3825–3828.
- Mastalerz, M., Hampton, L. B., Drobnik, A., & Loope, H. (2017). Significance of analytical particle size in low-pressure N₂ and CO₂ adsorption of coal and shale. *International Journal of Coal Geology*, 178(1), 122–131.
- Meng, Z. Y., Xu, G. S., Liu, Y., Yang, C., Yuan, H. F., & Liang, J. J. (2015). Hydrocarbon accumulation conditions of the weathering crust paleokarst gas reservoirs of Leikoupo Formation, west Sichuan, China. *Journal of Chengdu University of Technology (Science & Technology Edition)*, 42(01), 70–79.
- Pan, Y. S., Huang, Z. L., Guo, X. B., Liu, B. C., Wang, G. Q., & Xu, X. F. (2022). Study on the pore structure, fluid mobility, and oiliness of the lacustrine organic-rich shale affected by volcanic ash from the Permian Lucaogou Formation in the Santanghu Basin, Northwest China. *Journal of Petroleum Science and Engineering*, 208, 109351.
- Pan, Y. S., Huang, Z. L., Li, T. J., Xu, X. F., Chen, X., & Guo, X. B. (2021). Pore structure characteristics and evaluation of

- lacustrine mixed fine-grained sedimentary rocks: A case study of the Lucaogou Formation in the Malang Sag, Santanghu Basin, Western China. *Journal of Petroleum Science and Engineering*, 201, 108545.
- Pang, X. Q. (2016). *Genetic mechanism and prediction methodology for overstacked and continuous hydrocarbon accumulations*. Science Press.
- Pang, X. Q., Huang, H. D., Lin, C. S., Zhu, X. M., Liao, Y., Chen, J. F., Kang, Y. S., Bai, G. P., Wu, G. D., Wu, X. S., Yu, F. S., Jiang, F. J., & Xu, J. L. (2014). Formation, distribution, exploration, and resource/reserve assessment of superimposed continuous gas field in Marsel exploration area, Kazakhstan. *Acta Petrolei Sinica*, 35(06), 1012–1056.
- Pei, S. Q., Wang, X. Z., Li, R. R., Yang, X., Long, H. Y., Hu, X., & Wang, X. X. (2021). Burial dolomitization of marginal platform bank facies and its petroleum geological implications: The genesis of Middle Permian Qixia Formation dolostones in the northwestern Sichuan Basin. *Natural Gas Industry*, 41(04), 22–29.
- Peng, R. D., Yang, Y. C., Ju, Y., Mao, L. T., & Yang, Y. M. (2011). Fractal dimension calculation of rock pore based on gray CT image. *Chinese Science Bulletin*, 56(26), 2256–2266.
- Pfeifer, P., Obert, M., & Cole, M. W. (1990). Fractal BET and FHH theories of adsorption: A comparative study. *Proceedings of the Royal Society of London A*, 423, 169–188.
- Qiao, J. C., Zeng, J. H., Chen, D. X., Cai, J. C., Jiang, S., Xiao, E. Z., Zhang, Y. C., Feng, X., & Feng, S. (2022). Permeability estimation of tight sandstone from pore structure characterization. *Marine and Petroleum Geology*, 135, 105382.
- Qin, M. T., Xie, S. Y., Zhang, J. B., Zhang, T. F., Carranza, E. J. M., Li, H. J., & Ma, J. Y. (2021). Petrophysical texture heterogeneity of vesicles in andesite reservoir on micro-scales. *Journal of Earth Science*, 32(4), 799–808.
- Rashid, F., Hussein, D., Glover, P. W. J., Lorinczi, P., & Lawrence, J. A. (2022). Quantitative diagenesis: Methods for studying the evolution of the physical properties of tight carbonate reservoir rocks. *Marine and Petroleum Geology*, 139, 105603.
- Ren, Y. G., Wang, C., Wu, H. B., Yu, J., Shao, H. M., Wan, Z. M., Wang, G. S., & Guo, H. L. (2011). *Oil and gas industry standard of the People's Republic of China: Oil and gas reservoir evaluation method (SY/T 6285-2011)*. Petroleum Industry Press.
- Sahouli, B., Blacher, S., & Brouers, F. (1996). Fractal surface analysis by using nitrogen adsorption data: The case of the capillary condensation regime. *Langmuir*, 12(11), 2872–2874.
- Sakhaee-Pour, A., & Li, W. (2016). Fractal dimensions of shale. *Journal of Natural Gas Science and Engineering*, 30, 578–582.
- Shao, X. H., Pang, X. Q., Li, H., & Zhang, K. (2017). Fractal analysis of pore network in tight gas sandstones using NMR method: a case study from the Ordos Basin, China. *Energy and Fuels*, 31(10), 10358–10368.
- Shi, K. Y., Chen, J. Q., Pang, X. Q., Jiang, F. J., Hui, S. S., Pang, H., Ma, K. Y., & Cong, Q. (2022). Effect of wettability of shale on CO₂ sequestration with enhanced gas recovery in shale reservoir: Implications from molecular dynamics simulation. *Journal of Natural Gas Science and Engineering*, 107, 104798.
- Sok, R. M., Varslot, T., Ghous, A., Latham, S., & Knackstedt, M. A. (2010). Pore scale characterization of carbonates at multiple scales: Integration of micro-CT, BSEM, and FIBSEM. *Petrophysics*. <https://doi.org/10.2451/2010PM0023>.
- Sun, J., Dong, Z. Q., & Zhen, Q. (2005). Research status and development trend of dolomite genesis. *Natural Gas Geoscience*, 10, 25–30.
- Sun, M. D., Yu, B. S., Hu, Q. H., Chen, S., Xia, W., & Ye, R. C. (2016). Nanoscale pore characteristics of the Lower Cambrian Niutitang Formation Shale: A case study from Well Yuke #1 in the Southeast of Chongqing, China. *International Journal of Coal Geology*, 154–155(15), 16–29.
- Tan, Q. G., You, L. J., Kang, Y. L., & Xu, C. Y. (2021). Formation damage mechanisms in tight carbonate reservoirs: The typical illustrations in Qaidam Basin and Sichuan Basin, China. *Journal of Natural Gas Science and Engineering*, 95, 104193.
- Teegavarapu, R. S. V. (2019). Chapter 1—Methods for analysis of trends and changes in hydroclimatological time-series. In R. Teegavarapu (Ed.), *Trends and changes in hydroclimatic variables* (pp. 1–89). Elsevier. <https://doi.org/10.1016/B978-0-12-810985-4.00001-3>.
- Voss, R. F., Laibowitz, R. B., & Alessandrini, E. I. (1991). Fractal geometry of percolation in thin gold films. *Scaling phenomena in disordered systems* (p. 10.1007/978-1-4757-1402-9_23). Springer.
- Wang, J. L., Song, H. Q., & Wang, Y. H. (2020a). Investigation on the micro-flow mechanism of enhanced oil recovery by low-salinity water flooding in carbonate reservoir. *Fuel*, 266(15), 117156.
- Wang, L., He, Y. M., Peng, X., Deng, H., Liu, Y. C., & Xu, W. (2019). Pore structure characteristics of an ultradeep carbonate gas reservoir and their effects on gas storage and percolation capacities in the Deng IV member, Gaoshiti-Moxi Area, Sichuan Basin, SW China. *Marine and Petroleum Geology*, 111, 44–65.
- Wang, Y. C., Cao, J., Tao, K. Y., Li, E. T., Ma, C., & Shi, C. H. (2020b). Reevaluating the source and accumulation of tight oil in the middle Permian Lucaogou Formation of the Junggar Basin, China. *Marine and Petroleum Geology*, 117, 104384.
- Wang, Z. Y., Pan, M., Shi, Y. M., Liu, L., Xiong, F., & Qin, Z. (2018). Fractal analysis of Donghetang sandstones using NMR measurements. *Energy and Fuels*, 32, 2973–2982.
- Wei, D., Gao, Z. Q., Zhang, C., Fan, T. L., Karubandika, G. M., & Meng, M. M. (2019). Pore characteristics of the carbonate shoal from fractal perspective. *Journal of Petroleum Science and Engineering*, 174, 1249–1260.
- Wei, W., Azmy, K., & Zhu, X. M. (2022). Impact of diagenesis on reservoir quality of the lacustrine mixed carbonate-siliciclastic-volcaniclastic rocks in China. *Journal of Asian Earth Sciences*, 233, 105265.
- Westphal, H., Eberli, G. P., Smith, L. B., Grammer, G. M., & Kislak, J. (2004). Reservoir characterization of the Mississippian Madison Formation, Wind River Basin, Wyoming. *AAPG Bulletin*, 88(4), 405–432.
- Xie, S. Y., Cheng, Q. M., Ling, Q. C., Li, B., Bao, Z. Y., & Fan, P. (2010). Fractal and multifractal analysis of carbonate pore-scale digital images of petroleum reservoirs. *Marine and Petroleum Geology*, 27(2), 476–485.
- Xin, Y., Wang, G. W., Liu, B. C., Ai, Y., Cai, D. Y., Yang, S. W., Liu, H. K., Xie, Y. Q., & Chen, K. J. (2022). Pore structure evaluation in ultra-deep tight sandstones using NMR measurements and fractal analysis. *Journal of Petroleum Science and Engineering*, 211, 110180.
- Xoath, B. B. (1966). Coal and gas outburst. In S. Z. Song & Y. A. Wang (Eds.), *Translation*. Beijing: China Industry Press.
- Xu, G. F., Lin, C. S., & Li, Z. T. (2014a). Lithofacies paleogeography and favorable reservoir of Lower Carboniferous in southern Kazakhstan. *Journal of Northeast Petroleum University*, 38, 1–11.
- Xu, S., Gou, Q. Y., Hao, F., Zhang, B. Q., Shu, Z. G., & Zhang, Y. Y. (2020). Multiscale faults and fractures characterization and their effects on shale gas accumulation in the Jiaoshiba area, Sichuan Basin, China. *Journal of Petroleum Science and Engineering*, 189, 107026.
- Xu, Z. X., Guo, S. B., Q, H., & Li, H. M. (2014b). Research on fractal characteristics of micro pore structure for shale gas. *Unconventional Oil & Gas*, 1(02), 20–25.

- Yang, C., Xiong, Y. Q., & Zhang, J. C. (2020). A comprehensive re-understanding of the OM-hosted nanopores in the marine Wufeng–Longmaxi shale formation in South China by organic petrology, gas adsorption, and X-ray diffraction studies. *International Journal of Coal Geology*, 218, 103362.
- Yang, F., Ning, Z. F., & Liu, H. Q. (2014). Fractal characteristics of shales from a shale gas reservoir in the Sichuan Basin, China. *Fuel*, 115, 378–384.
- Zambrano, M., Tondi, E., Mancini, L., Arzilli, F., Lanzafame, G., Materazzi, M., & Torrieri, S. (2017). 3D Pore-network quantitative analysis in deformed carbonate grainstones. *Marine and Petroleum Geology*, 82, 251–264.
- Zhang, J. Z., Tang, Y. J., He, D. X., Sun, P., & Zou, X. Y. (2020a). Full-scale nanopore system and fractal characteristics of clay-rich lacustrine shale combining FE-SEM, nano-CT, gas adsorption and mercury intrusion porosimetry. *Applied Clay Science*, 196, 105758.
- Zhang, K., Pang, X. Q., Zhao, Z. F., Shao, X. H., Zhang, X., Li, W., & Wang, K. (2018). Pore structure and fractal analysis of Lower Carboniferous carbonate reservoirs in the Marsel area, Chu-Sarysu basin. *Marine and Petroleum Geology*, 93, 451–467.
- Zhang, M. L., Lin, C. S., Sun, Y. D., Liu, J. Y., Li, H., Wang, Q. L., & Wang, Y. (2020b). Sequence framework, depositional evolution and controlling processes, the Early Carboniferous carbonate system, Chu-Sarysu Basin, southern Kazakhstan. *Marine and Petroleum Geology*, 111, 544–556.
- Zhang, X. W., Pang, X. Q., Jin, Z. K., Hu, T., Toyin, A., & Wang, K. (2020c). Depositional model for mixed carbonate-clastic sediments in the Middle Cambrian Lower Zhangxia Formation, Xiaweidian, North China. *Advances in Geo-Energy Research*, 4(1), 29–42.
- Zhang, Y. X., Yang, S. L., Zhang, Z., Li, Q., Deng, H., Chen, J. Y., Geng, W. Y., Wang, M. Y., Chen, Z. X., & Chen, H. (2022). Multiscale pore structure characterization of an ultra-deep carbonate gas reservoir. *Journal of Petroleum Science and Engineering*, 208, 109751.
- Zhao, P. Q., Wang, Z. L., Sun, Z. C., Cai, J. C., & Wang, L. (2017a). Investigation on the pore structure and multifractal characteristics of tight oil reservoirs using NMR measurements: Permian Lucaogou Formation in Jimusaer Sag, Junggar Basin. *Marine and Petroleum Geology*, 86, 1067–1081.
- Zhao, Z. F., Pang, X. Q., Li, Q. W., Hu, T., Wang, K., Li, W., Guo, K. Z., Li, J. B., & Shao, X. H. (2017b). Depositional environment and geochemical characteristics of the Lower Carboniferous source rocks in the Marsel area, Chu-Sarysu Basin, Southern Kazakhstan. *Marine and Petroleum Geology*, 81, 134–148.
- Zhou, J. G., Xu, C. C., Yao, G. S., Yang, G., Zhang, J. Y., Hao, Y., Wang, F., Pan, L. G., Gu, M. F., & Li, W. Z. (2015). Genesis and evolution of Lower Cambrian Longwangmiao Formation reservoirs, Sichuan Basin, SW China. *Petroleum Exploration and Development*, 42(2), 158–166.
- Zhou, X. X., Lü, X. X., Sui, F. G., Wang, X. J., & Li, Y. Z. (2021). The breakthrough pressure and sealing property of Lower Paleozoic carbonate rocks in the Gucheng area of the Tarim Basin. *Journal of Petroleum Science and Engineering*, 208, 109289.

Springer Nature or its licensor (e.g. a society or other partner) holds exclusive rights to this article under a publishing agreement with the author(s) or other rightsholder(s); author self-archiving of the accepted manuscript version of this article is solely governed by the terms of such publishing agreement and applicable law.